Regional-scale chemical transport modeling in support of the analysis of observations obtained during the TRACE-P experiment

G. R. Carmichael,[1] Y. Tang,[1] G. Kurata,[3] I. Uno,[2] D. Streets,[4] J.-H. Woo,[1] H. Huang,[1] J. Yienger,[1] B. Lefer,[5] R. Shetter,[5] D. Blake,[6] E. Atlas,[5] A. Fried,[5] E. Apel,[5] F. Eisele,[5] C. Cantrell,[5] M. Avery,[7] J. Barrick,[7] G. Sachse,[7] W. Brune,[8] S. Sandholm,[9] Y. Kondo,[10] H. Singh,[11] R. Talbot,[12] A. Bandy,[13] D. Thorton,[13] A. Clarke,[14] and B. Heikes[15]

[1] Data obtained during the TRACE-P experiment is used to evaluate how well the CFORS/STEM-2K1 regional-scale chemical transport model is able to represent the aircraft observations. Thirty-one calculated trace gas and aerosol parameters are presented and compared to the in situ data. The regional model is shown to accurately predict many of the important features observed. The mean values of all the model parameters in the lowest 1 km are predicted within ±30% of the observed values. The correlation coefficients (R) for the meteorological parameters are found to be higher than those for the trace species. For example, for temperature, R > 0.98. Among the trace species, ethane, propane, and ozone show the highest values (0.8 < R < 0.9), followed by CO, SO_2, and NO_y. NO and NO_2 had the lowest values (R < 0.4). Analyses of pollutant transport into the Yellow Sea by frontal events are presented and illustrate the complex nature of outflow. Biomass burning from SE Asia is transported in the warm conveyor belt at altitudes above ∼2 km and at latitudes below 30N. Outflow of pollution emitted along the east coast of China in the postfrontal regions is typically confined to the lower ∼2 km and results in high concentrations with plume-like features in the Yellow Sea. During these situations the model underpredicts CO and black carbon (among other species). An analysis of ozone production in this region is also presented. In and around the highly industrialized regions of East Asia, where fossil fuel usage dominates, ozone is NMHC-limited. South of ∼30–35N, ozone production is NO_x-limited, reflecting the high NMHC/NO_x ratios due to the large contributions to the emissions from biomass burning, biogenics sources, and biofuel usage in central China and SE Asia. *INDEX TERMS:* 0322 Atmospheric Composition and Structure: Constituent sources and sinks; 0365 Atmospheric Composition and Structure: Troposphere—composition and chemistry; 0345 Atmospheric Composition and Structure: Pollution—urban and regional (0305)

1. Introduction

[2] Chemical Transport Models (CTMs) are playing increasingly important roles in the design, execution, and analysis of large-scale atmospheric chemistry field studies.

The use of global CTMs in chemical weather forecasting applications in support of stratospheric field experiments began in the mid-1990s [*Lee et al.*, 1997], while global CTM forecasts were introduced in the Indian Ocean Exper-

[1]Center for Global and Regional Environmental Research, University of Iowa, Iowa City, Iowa, USA.

[2]Research Institute for Applied Mechanics, Kyushu University, Fukuoka, Japan.

[3]Department of Ecological Engineering, Toyohashi University of Technology, Toyohashi, Japan.

[4]Decision and Information Sciences Division, Argonne National Laboratory, Argonne, Illinois, USA.

[5]National Center for Atmospheric Research, Boulder, Colorado, USA.

[6]Department of Chemistry, University of California, Irvine, Irvine, California, USA.

[7]NASA Langley Center, Hampton, Virginia, USA.

[8]Department of Meteorology, Pennsylvania State University, University Park, Pennsylvania, USA.

[9]Georgia Institute of Technology, Atlanta, Georgia, USA.

[10]Research Center for Advanced Science and Technology, University of Tokyo, Tokyo, Japan.

[11]NASA Ames Research Center, Moffett Field, California, USA.

[12]Institute for the Study of Earth, Oceans, and Space, University of New Hampshire, Durham, New Hampshire, USA.

[13]Chemistry Department, Drexel University, Philadelphia, Pennsylvania, USA.

[14]School of Ocean and Earth Science and Technology, University of Hawaii at Manoa, Honolulu, Hawaii, USA.

[15]Graduate School of Oceanography, University of Rhode Island, Kingston, Rhode Island, USA.
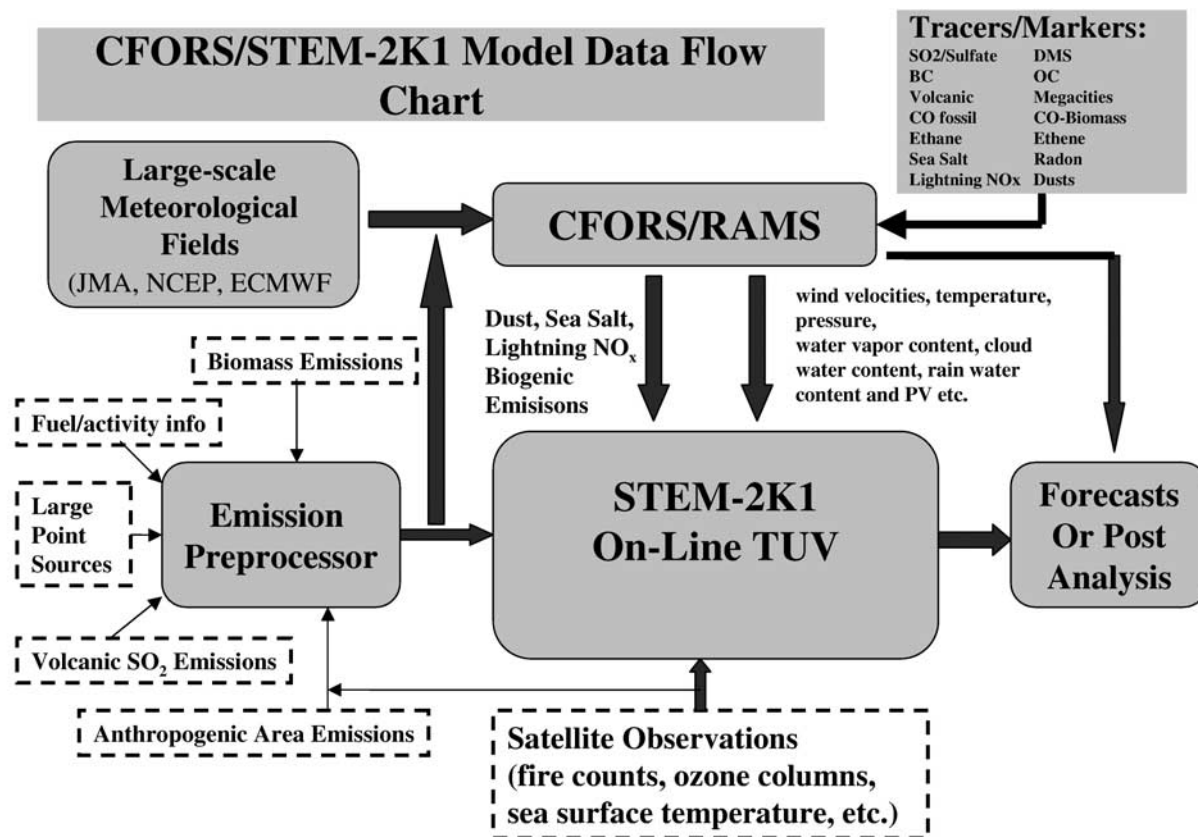
Figure 1. Schematic diagram of the CFORS/STEM-2K1 regional-scale modeling system used in support of the TRACE-P experiment.

iment (INDOEX) [*Collins et al.*, 2001; *Rasch et al.*, 2001]. CTMs have now become an integral part of large of large field experiments (see *Lawrence et al.* [2002] and references therein for an excellent summary of CTMs used in chemical weather forecasting activities associate with several recent field experiments). They are being used in forecast mode to enhance flight planning by enabling the representation of important three-dimensional atmospheric chemical structures (such as dust storm plumes, polluted air masses associated with large cities, and widespread biomass burning events) and how they evolve over time. CTM forecasts play the additional important role of providing a four-dimensional (4-D) contextual representation of the experiment. CTMs also facilitate the integration of the different measurements and measurement platforms (e.g., aircraft, ground stations, and satellite observations). Finally, CTMs can be used to help evaluate and improve emission estimates.

[3] We developed an operational regional-scale forecasting and analysis system to assist in atmospheric field experiments. The Chemical Weather Forecasting System (CFORS) consists of three major components: (1) detailed mesoscale meteorological model with on-line air mass and emission tracers; (2) detailed 3-D photochemical calcula-

tions using CTMs; and (3) an emissions module that intimately links emitted amounts and source activities to the transport and chemistry analysis. CFORS was applied for the first time in the design and execution of the NASA TRACE-P (Transport and Chemical Evolution over the Pacific) [*Jacob et al.*, 2003] and NSF ACE-Asia (Aerosols Characterization Experiment in Asia) [*Huebert et al.*, 2003] intensive field experiments. The TRACE-P experiment was the first application of this model. The TRACE-P data provide an excellent opportunity to test the capabilities of this model to represent important observed features of trace gas distributions in the western Pacific. In this paper we present a brief overview of the CFORS system and results obtained using the STEM-2K1 CTM. We focus our analysis and discussion on three questions: (1) How well did our regional CTM and estimated emissions represent the observations?; (2) How can the model, by providing temporal and spatial context, aid in the interpretation of the aircraft observations?; and (3) What do these results tell us about our capabilities to characterize ozone production in East Asia, and how changing trends in emissions may alter ambient ozone levels?

[4] The paper is structured as follows. The model system is briefly introduced in section 2, along with information on

Figure 2. Forecasts of pollution outflow during the frontal events of 2 March (top left) through 10 March (lower right). Shown are clouds (white), BC isosurface (>1 μg/m3) colored by percent due to biomass burning (red > 50%), 3 km streamlines (orange), wind vectors at 600 m (blue) at 6 GMT. The green-brown-gray shading represents the topography in the region (from low to high). The Tibet Plateau is white in these images. See color version of this figure at back of this issue.

the emissions used in the analysis. The comparison of model results with observations is presented in section 3. We first present a mission-wide perspective of how well the model was able to reproduce observed latitude and altitude features, and then we present a comparison with the observations of all the model parameters that were also observed. In this section we also present a detailed analysis of pollutant transport in frontal outflow events and highlight how emissions from Southeast and East Asia were sampled by the aircrafts at different altitudes. We then present an analysis of how the model can be used to characterize the impact of the sampling strategy used in TRACE-P on regional budgets. Finally, we discuss how the results can be used to characterize ozone production in East Asia.

2. Model Description

[5] An overview of the CFORS/STEM-2K1 modeling system as used in TRACE-P and ACE-Asia experiments is shown in Figure 1. Shown are the main system elements and data exchanges. CFORS is a multitracer, on-line system built within the RAMS mesoscale meteorological model [*Pielke et al.*, 1992]. An important feature of CFORS is that multiple tracers are run on-line in RAMS so that all the on-line meteorological information such as 3-D winds, boundary-layer turbulence, surface fluxes, and precipitation amount are directly used by the tracer model at every time step. As a result, CFORS produces with high time resolution 3-D fields of tracer distributions and major meteorological parameters. CFORS includes a wide variety of tracers to help characterize air masses. These include: (1) important anthropogenic species (SO_2/SO_4, CO, black carbon, organic carbon, fast and slow reacting hydrocarbons, and NO_x); (2) species of natural origin (yellow sand, sea salt, radon, volcanic SO_2); and (3) markers for biomass burning (CO, black carbon, and organic carbon) and megacities. CFORS/on-line forecasts consist of gas and aerosol mass distributions and meteorological parameters. For the analysis of reactive species, a CTM is used. CFORS is designed to interface with various CTMs. In this paper we discuss results using the STEM model. Results based on the CMAQ CTM are presented by *Zhang et al.* [2003]. The STEM version used is referred to as the 2K1 (2001) version

Table 1. Emissions Used in This Study in Units of Gg/March, Tg/March (CO_2)[a]

	China			Other East Asia			Southeast Asia			South Asia			Total		
	Ant[b]	BB[c]	Total	Ant.	BB	Total	Ant.	BB	Total	Ant.	BB	Total	Ant.	BB	Total
SO_2	1724.3	12.1	1736.4	196.5	0.8	197.2	267.5	57.6	325.2	602.7	25.7	628.4	2791.0	96.2	2887.2
NO_x	894.4	105.8	1000.2	367.4	6.4	373.9	259.7	364.2	623.9	404.2	182.3	586.6	1925.7	658.8	2584.5
CO	8493.6	2463.0	10956.6	1276.5	131.3	1407.8	2891.5	10760.2	13651.6	5286.7	4385.9	9672.6	17948.3	17740.4	35688.6
CH_4	3129.1	85.9	3215.0	370.0	4.6	374.6	1656.4	624.9	2281.3	3469.0	166.2	3635.2	8624.6	881.6	9506.2
NH_3	1133.3	34.5	1167.8	75.0	1.8	76.8	251.4	141.1	392.5	799.8	60.2	860.0	2259.4	237.6	2497.1
CO_2	300.1	41.2	341.3	164.8	2.3	167.1	99.6	177.7	277.3	172.6	70.7	243.4	737.2	291.9	1029.1
BC	79.5	17.7	97.2	8.8	0.9	9.7	27.2	70.9	98.1	56.0	29.6	85.6	171.5	119.1	290.7
OC	225.7	104.0	329.7	16.6	7.0	23.6	116.4	525.9	642.3	239.1	225.6	464.7	597.8	862.5	1460.3
PM_{10}	933.2	339.0	1272.2	74.4	19.1	93.4	366.1	1165.3	1531.3	1114.7	622.9	1737.5	2488.2	2146.2	4634.4
$PM_{2.5}$	508.6	137.9	646.5	39.9	9.6	49.5	226.2	887.3	1113.5	688.5	309.2	997.8	1463.3	1344.0	2807.2
Ethane	69.4	26.7	96.1	5.7	1.2	6.9	57.1	126.1	183.3	59.4	43.5	102.8	191.6	197.4	389.0
Propane	51.5	12.5	64.0	7.8	0.6	8.3	28.4	21.9	50.3	33.2	19.5	52.6	120.8	54.5	175.3
Butane	75.3	2.0	77.3	35.1	0.1	35.2	41.2	6.5	47.7	51.2	3.6	54.9	202.8	12.3	215.1
Pentane	56.4	0.7	57.1	15.6	0.0	15.7	30.1	1.7	31.8	38.2	1.4	39.6	140.3	3.9	144.2
Other Alkane	154.2	6.4	160.7	59.7	0.3	60.1	122.5	25.6	148.1	92.9	11.0	103.9	429.3	43.4	472.7
Ethene	130.2	40.6	170.8	11.4	1.9	13.3	110.8	212.0	322.8	123.8	67.8	191.6	376.2	322.3	698.5
Propene	48.3	25.3	73.6	5.8	1.2	6.9	43.7	67.3	111.0	46.5	40.3	86.8	144.3	134.1	278.3
T. Alkene[d]	34.8	12.8	47.7	4.6	0.8	5.4	29.3	64.5	93.8	30.7	25.1	55.8	99.5	103.2	202.7
I. Alkene[d]	53.2	3.5	56.7	5.3	0.2	5.5	47.7	19.5	67.2	53.5	6.4	59.9	159.7	29.7	189.3
Ethyne	70.2	10.3	80.5	4.8	0.5	5.3	47.4	46.4	93.9	56.7	16.8	73.5	179.1	74.0	253.2
Benzene	53.8	5.7	59.5	3.3	0.4	3.7	62.2	42.3	104.5	50.8	12.5	63.3	170.0	60.9	230.9
Toluene	115.6	2.7	118.3	28.0	0.3	28.3	70.6	29.5	100.1	57.4	8.1	65.5	271.5	40.6	312.1
Xylene	44.3	0.9	45.2	10.2	0.1	10.3	24.5	6.4	30.9	23.2	2.9	26.1	102.2	10.3	112.5
Other Aromatics	86.8	2.6	89.4	17.3	0.2	17.4	62.9	9.6	72.5	55.2	5.5	60.7	222.2	17.8	240.0
HCHO	14.3	39.6	53.9	4.4	2.1	6.5	9.1	149.9	159.1	10.1	75.2	85.3	37.9	266.8	304.7
Other Aldehydes	20.6	27.8	48.3	1.2	1.5	2.7	18.5	119.7	138.2	20.9	49.0	69.9	61.2	197.9	259.1
Ketones	12.8	56.5	69.4	5.9	2.9	8.8	6.7	233.0	239.7	3.8	97.2	101.0	29.3	389.6	418.8
Halocarbones	16.4	5.7	22.1	9.2	0.2	9.5	9.0	7.0	16.0	4.8	8.2	13.1	39.5	21.2	60.7
Other NMVOCs[e]	160.6	145.3	305.9	86.4	9.1	95.5	129.9	750.1	879.9	102.7	299.0	401.7	479.6	1203.4	1683.0

[a]Each chemical species is represented as full molecular weight, with the exception of NO_x, which is represented as NO_2.
[b]Anthropogenic emissions including biofuel combustions.
[c]Biomass "open" burning emissions (forest, grassland/savanna, and agricultural residue burning).
[d]Terminal alkenes and internal alkenes.
[e]Any organic compounds not in the main 18 NMVOCs classes (such as acids, alcohols, ethers, etc.).

(thus STEM-2K1). CFORS provides the meteorological fields used by STEM, and then STEM calculates the transport, chemistry, removal, and photolysis processes. The emission preprocessor provides detailed information on total emissions, including information on emissions by source sector and fuels, and this information is used by both the CFORS/on-line and STEM. Additional external data needed by the system is also shown in Figure 1. This includes satellite data on fire counts, column ozone, and sea surface temperatures. Further details regarding the model elements are presented below.

2.1. CFORS Forecast Operations

[6] During the TRACE-P and ACE-Asia intensive observations, CFORS was run in an operational forecasting mode and provided daily forecasts of meteorology and gas/aerosol distributions. A unique element of the operational model was that two separate forecasts were produced each day; one where the RAMS model was initialized by the NCEP (National Center for Environmental Prediction/NOAA) 96 hour forecasting AVN data set http://www.emc.ncep.noaa. gov/modelinfo/index.html); and the second using JMA (Japan Meteorological Agency) 72 hour forecasting ASIA domain data set http://ddb.kishou.go.jp/). For each day the following 72-hour products were provided: (1) CFORS/ on-line forecasts of meteorological and tracer fields for both JMA and NCEP initializations; (2) photochemical fields using the RAMS fields to drive STEM-2K1 at 80 km; and (3) same as 2 but for 16 km horizontal resolution. After the

field campaigns, the CFORS system was applied in hindcast mode using ECMWF global meteorological data set (6 hour interval with $1° × 1°$ resolution), analyzed weekly SST (sea surface temperature) data, and observed monthly snow-cover information as the boundary conditions for the RAMS calculations.

[7] The numerical model domain for the analysis (both CFORS and STEM) was centered at 25N 115E with a horizontal grid of 100 by 90 grid points and a resolution of 80 km. In the vertical, the domain was divided into 23 layers (nonuniformly spaced layers ranging in depth from 150 m to 1800 m), with the top level at 23 km. All calculations were performed on Linux clusters and results were made available via the CFORS web manager. The CGI interactive interface can plot 2-D of fields and time-height cross-sections at fixed points according to user's requests. Quick-look vis5D 3-D animations were also provided. The CFORS web site can be accessed at http://cfors.riam. kyushu-u.ac.jp/~cforsdemo/index.html. Further details regarding the CFORS/on-line are presented in the work of *Uno et al.* [2003].

[8] Sample results of the CFORS/on-line tracer forecasts, as used in flight planning, are presented in Figure 2. Shown are snapshots at 6 GMT of pollution outflow during the frontal events of 2 March (top left) through 10 March (lower right). Depicted in these figures are: clouds (white); BC isosurface (>1 μg/m3) colored by percent due to biomass burning (red > 50%); 3 km streamlines (orange); and wind vectors at 600 m (blue). These scenes show how pollutants
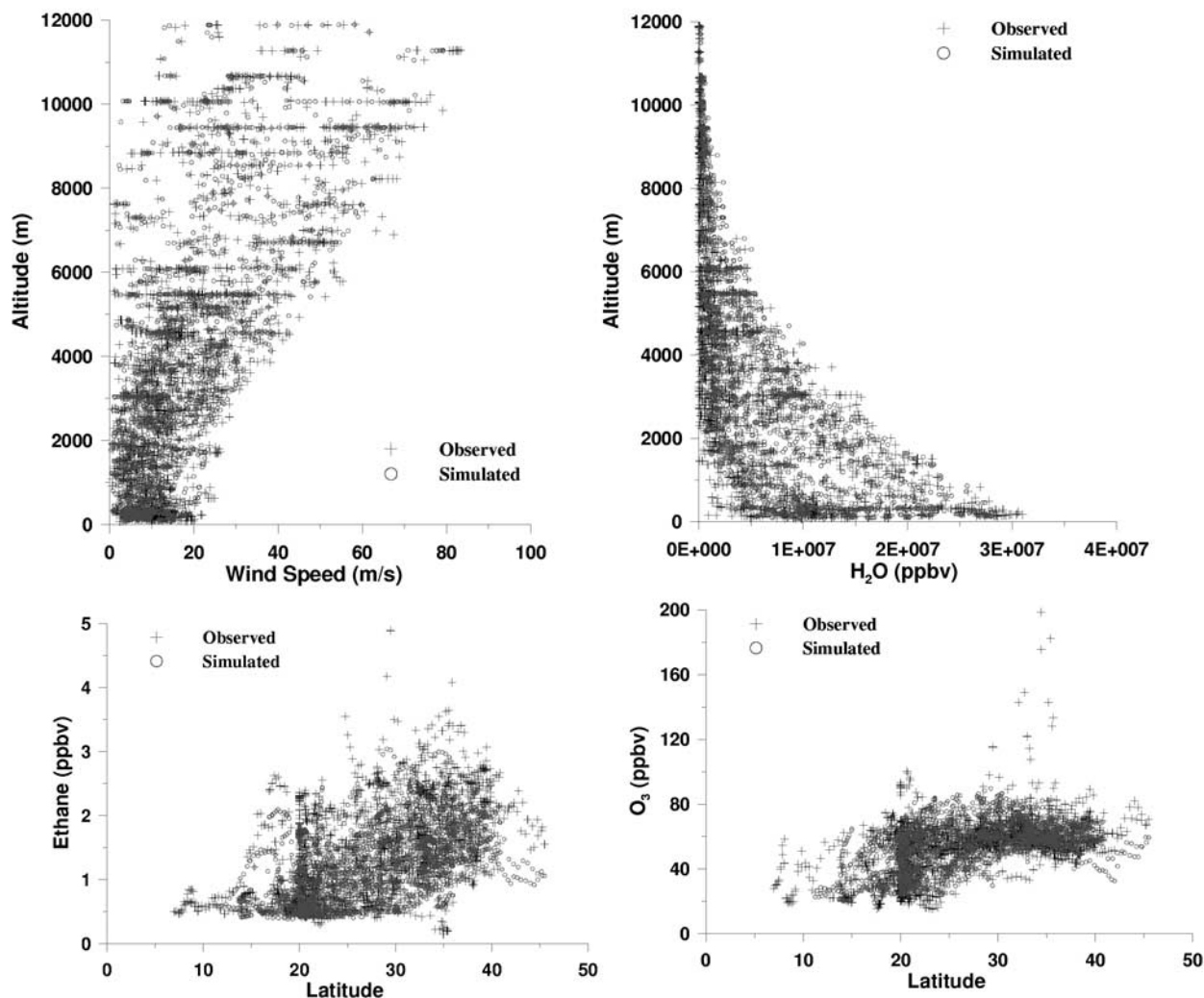
Figure 3. Measured and modeled vertical distributions of wind speed and water vapor mixing ratios (top) and latitudinal distributions of ethane and ozone (bottom) for the DC8 and P-3B aircraft data. Shown are values for each 5-min flight segments from the merged data set. See color version of this figure at back of this issue.

emitted from different source areas are transported off the continent by traveling low-pressure systems. For example, the top row shows how black carbon is transported by low-pressure systems as they sweep across northern China, the Korean peninsula, and Japan. The first frame (upper right) shows remnants of an earlier front (white clouds in the far right of the domain) and a low-pressure system over Mongolia (top middle). A BC-rich air mass was transported in the postfrontal region (of the first front) into the Yellow Sea. This air mass is confined to the lowest 2 km and is due largely to anthropogenic emissions from eastern China (as indicated by the blue color). As the low moves to the east (top middle frame) BC from biomass burning (the red shaded area) in Southeast Asia is transported towards the center of the low along the warm sector of the front. In the warm sector the BC-rich air mass is transported at altitudes above 3 km (as seen by the fact that the BC air mass has features that extend above the 3 km streamlines). Below 2 km

BC is also elevated, but this BC is due to anthropogenic sources (as shown by the blue shaded area below the red). During 7–10 March the DC-8 and P-3B sampled pollution outflow as this cold front swept over East Asia. The findings from these missions are discussed in the Results section.

2.2. STEM-2K1

[9] The meteorological fields and those emissions estimated in an on-line manner inside of CFORS were used to drive the STEM-2K1 model, which then produced estimated fields of primary and secondary chemical and aerosol constituents. This model is an enhanced version of the STEM model [*Song and Carmichael*, 2001]. The important new features in STEM-2K1 include: (1) the use of the SAPRC99 chemical mechanism [*Carter*, 2000], which consists of 93 species and 225 reactions; (2) the integration of the chemical mechanism using and the implicit second order Rosenbrock method [*Verwer et al.*, 1999]; (3) the

Table 2. Observed and Calculated Values of Parameters Modeled by the CFORS/STEM-2K1 for TRACE-P DC-8 Flights 6 to 17

Species and Variables	Below 1 km			1 km to 3 km			Above 3 km		
	Observed	Modeled	R	Observed	Modeled	R	Observed	Modeled	R
Wind Speed, m/s	8.3	7.6	0.84	11.1	10.9	0.89	31.9	31.3	0.98
Temperature, K	288.3	287.5	0.99	278.3	277.4	0.99	248.7	250.1	0.99
H_2O, ppmv	1399.2	1408.6	0.98	6527.9	6977.3	0.96	1117.4	1534.1	0.91
CO, ppbv	218.8	203.8	0.76	188.3	195.1	0.55	122.4	121.2	0.62
O_3, ppbv	51.1	51.3	0.81	52.8	52.9	0.73	61.4	59.9	0.28
Ethane, ppbv[a]	1.9	1.6	0.89	1.7	1.4	0.81	0.9	0.8	0.74
Propane, ppbv[a]	0.63	0.44	0.84	0.48	0.39	0.73	0.15	0.18	0.71
Ethyne, ppbv[a]	0.79	0.60	0.68	0.55	0.49	0.64	0.25	0.20	0.60
Ethene, ppbv[a]	0.18	0.15	0.68	0.11	0.11	0.37	0.033	0.025	0.48
SO_2, ppbv	1.6	1.0	0.68	0.7	1.0	0.27	0.19	0.10	0.68
SO_4, ppbv	1.6	1.4	0.68	0.8	1.1	0.49	0.2	0.2	0.72
Acetone, ppbv[b]	1.3	1.4	0.59	1.2	1.3	0.39	1.0	0.9	0.37
Acetone-Singh, ppbv[c]	0.9	1.3	0.54	0.9	1.3	0.46	0.7	0.9	0.56
PAN, ppbv	0.55	0.50	0.81	0.31	0.44	0.67	0.19	0.13	0.55
NO_2, ppbv	0.27	0.30	0.24	0.12	0.30	0.31	0.034	0.007	0.075
NO, ppbv	0.036	0.054	0.45	0.034	0.046	0.09	0.053	0.008	0.21
RNO_3, ppbv[a]	0.046	0.067	0.83	0.031	0.050	0.80	0.012	0.014	0.73
Methyl Ethyl Ketone, ppbv[b]	0.24	0.21	0.58	0.19	0.18	0.37	0.077	0.071	0.51
H_2O_2, ppbv	0.85	1.05	0.54	1.11	1.16	0.56	0.43	0.49	0.55
Formaldehyde, ppbv[d]	0.60	0.62	0.69	0.33	0.47	0.40	0.10	0.13	0.61
Acetaldehyde, ppbv[b]	0.81	0.38	−0.24	0.55	0.35	−0.22	0.30	0.18	0.10
Acetaldehyde-Singh, ppbv[c]	0.48	0.38	0.58	0.32	0.35	0.44	0.14	0.18	0.61
OH, pptv	0.11	0.10	0.61	0.11	0.13	0.82	0.11	0.13	0.69
HO_2, pptv	10.4	10.4	0.68	11.7	13.0	0.86	8.7	11.5	0.85
Benzene + Toluene, ppbv	0.33	0.14	0.56	0.18	0.12	0.53	0.053	0.032	0.61
BC, ug/std m3[e]	0.84	0.69	0.63	0.84	0.59	0.23	0.26	0.17	0.34
AOE @550nm,/km[e]	0.062	0.072	0.64	0.039	0.053	0.34	0.0068	0.0086	0.58
$J[NO_2]$, 1/s	1.95×10^{-5}	1.19×10^{-5}	0.84	2.78×10^{-5}	1.93×10^{-5}	0.86	4.15×10^{-5}	3.22×10^{-5}	0.93
$J[O_3 \rightarrow O_2 + O^1D]$, 1/s	3.94×10^{-6}	2.84×10^{-6}	0.76	5.85×10^{-6}	4.85×10^{-6}	0.79	8.41×10^{-6}	7.73×10^{-6}	0.84
$J[H_2O_2]$, 1/s	3.57×10^{-7}	2.47×10^{-7}	0.80	5.19×10^{-7}	4.09×10^{-7}	0.83	7.21×10^{-7}	6.37×10^{-7}	0.80
$J[HNO_3]$, 1/s	1.21×10^{-3}	0.76×10^{-3}	0.74	1.81×10^{-3}	1.31×10^{-3}	0.74	2.58×10^{-3}	2.06×10^{-3}	0.73
$J[HNO_2 \rightarrow OH + NO]$, 1/s	1.75×10^{-5}	1.22×10^{-5}	0.77	2.68×10^{-5}	2.14×10^{-5}	0.80	4.36×10^{-5}	3.76×10^{-5}	0.86
$J[HCHO \rightarrow H + HCO]$, 1/s	2.63×10^{-5}	1.77×10^{-5}	0.75	4.12×10^{-5}	3.11×10^{-5}	0.77	6.92×10^{-5}	5.22×10^{-5}	0.81
$J[HCHO \rightarrow H_2 + CO]$, 1/s	2.30×10^{-6}	2.02×10^{-6}	0.80	4.08×10^{-6}	4.05×10^{-6}	0.83	1.13×10^{-5}	1.19×10^{-5}	0.93
$J[CH3CHO \rightarrow CH_3 + HCO]$, 1/s	2.91×10^{-7}	2.47×10^{-7}	0.81	5.11×10^{-7}	4.87×10^{-7}	0.84	1.41×10^{-6}	1.42×10^{-6}	0.94
$J[Acetone]$, 1/s	1.95×10^{-5}	1.19×10^{-5}	0.84	2.78×10^{-5}	1.93×10^{-5}	0.86	4.15×10^{-5}	3.22×10^{-5}	0.93

[a]Ethane, propane, ethyne, ethene and RNO_3 presented here were measured by *Blake and Atlas* [2003]. Observed RNO_3 here is the sum of observed 2-BuONO₂, 2-PeONO₂, 3-PeONO₂, n-PrONO₂, i-PrONO₂, MeONO₂, and EtONO₂.

[b]Acetone, acetaldehyde and methyl ethyl ketone measured by *Apel* [2003].

[c]Acetone and acetaldehyde measured by *Singh et al.* [2003].

[d]Formaldehyde by *Fried et al.* [2003].

[e]The black carbon is derived from aerosol absorption. The aerosol extinction coefficient (AOE) is the sum of aerosol absorption at 565 nm and aerosol scattering at 550 nm.

calculation of photolysis rates on-line, considering the influences of cloud, aerosol and gas-phase absorptions due to O_3, SO_2, and NO_2, using the NCAR Tropospheric Ultraviolet-Visible (TUV) radiation model [*Madronich and Flocke*, 1999]; and (4) the extension of the aerosol calculations to include optical information (e.g., extinction) in addition to mass, size, and composition. Details regarding the radiative transfer calculations are presented by *Tang et al.* [2003a]. Boundary conditions were selected based on observational data, and they were set to the lowest 5% at each altitude of the values observed during the TRACE-P operations in the western Pacific.

2.3. Emissions

[10] An important aspect of the CFORS system is that emissions development and analysis are coupled to the modeling activities. The anthropogenic emission inventories (SO_x, NO_x, CO, CO_2, NH_3, black carbon, organic carbon, and hydrocarbons) were prepared specifically for the TRACE-P and ACE-Asia experiments. A unique aspect of this bottom-up inventory is that it is driven by regional-specific information on fuels and activity. Biofuels and fossil fuels can be tracked separately, as can emissions from various economic sectors (e.g., domestic, transport, power generation, industrial). Emissions from specific regions and even megacities can be isolated. The details of the inventory are presented by *Streets et al.* [2003a, 2003b] and *Woo et al.* [2003].

[11] Emissions of lightning NO_x, dust, and sea salt are calculated on-line in CFORS. Further details pertaining to the dust emission technique are presented by *Uno et al.* [2003]. Sea salt can play an important role in radiative transfer. Sea salt emissions and transport processes are treated using two size modes within the CFORS framework. Sea salt emissions are calculated on-line based on the work of *Gong et al.* [1997]. Lighting NO_x is included as a tracer to provide estimates of air masses impacted by lightning. Lightning NO_x emissions are calculated on-line based on estimates of subgrid scale cumulus activity calculated by a simplified Kuo cumulus scheme. Lightning NO_x emissions are distributed vertically between cloud base and cloud top as discussed by *Pickering et al.* [1998].

Table 3. Observed and Calculated Values of Parameters Modeled by the CFORS/STEM-2K1 for TRACE-P P-3B Flights 8 to 19

Species and Variables	Below 1 km			1 km to 3 km			Above 3 km		
	Observed	Modeled	R	Observed	Modeled	R	Observed	Modeled	R
Wind Speed, m/s	10.8	9.4	0.88	10.3	10.3	0.91	17.7	17.9	0.95
Temperature, K	287.2	286.1	0.99	279.9	278.4	0.99	266.4	266.3	0.99
H_2O, ppmv	12646.1	12819.1	0.97	7594.4	7881.1	0.95	2651.9	3419.1	0.86
CO, ppbv	235.3	219.5	0.71	208.1	209.9	0.53	136.1	148.6	0.75
O_3, ppbv	55.5	56.4	0.88	55.4	53.4	0.60	52.6	48.8	0.62
Ethane, ppbv	2.2	1.7	0.70	1.6	1.5	0.64	1.1	1.1	0.77
Propane, ppbv	0.73	0.52	0.73	0.43	0.42	0.58	0.2	0.25	0.71
Ethyne, ppbv	0.79	0.69	0.68	0.59	0.54	0.39	0.3	0.3	0.49
Ethene, ppbv	0.14	0.13	0.75	0.09	0.11	0.39	0.033	0.034	0.36
SO_2, ppbv	2.1	2.8	0.80	0.54	1.42	0.45	0.19	0.23	0.57
SO_4, ppbv	1.6	2.1	0.82	0.66	1.43	0.53	0.13	0.43	0.21
HNO_3, ppbv	0.38	0.89	0.22	0.27	0.71	0.23	0.17	0.16	0.31
PAN, ppbv	0.54	0.66	0.78	0.37	0.51	0.65	0.19	0.18	0.71
NO_2, ppbv	0.43	0.41	0.09	0.40	0.25	0.37	0.04	0.011	0.31
NO, ppbv	0.08	0.08	0.07	0.057	0.053	0.17	0.021	0.007	0.36
RNO_3, ppbv[a]	0.056	0.085	0.65	0.031	0.057	0.72	0.015	0.018	0.70
NO_y, ppbv	1.6	2.5	0.69	1.4	1.91	0.43	0.51	0.49	0.60
Benzene + Toluene, ppbv	0.28	0.15	0.64	0.21	0.12	0.42	0.068	0.042	0.46
OH, pptv	0.21	0.11	0.54	0.20	0.16	0.83	0.17	0.14	0.85
HO_2, pptv	13.7	11.4	0.69	19.4	15.8	0.23	20.9	14.4	0.33
$HO_2 + RO_2$, pptv	21.2	19.0	0.76	34.8	26.15	0.72	27.1	25.2	0.63
AOE @550 nm,/km[b]	0.081	0.093	0.53	0.04	0.059	0.30	0.0095	0.019	0.41
$J[NO_2]$, 1/s	0.0061	0.0048	0.70	0.009	0.0081	0.73	0.011	0.010	0.71
$J[O_3 \rightarrow O_2 + O^1D]$, 1/s	1.9×10^{-5}	1.3×10^{-5}	0.80	3.4×10^{-5}	2.6×10^{-5}	0.87	4.1×10^{-5}	3.2×10^{-5}	0.91
$J[H_2O_2]$, 1/s	4.2×10^{-6}	3.4×10^{-6}	0.72	6.8×10^{-6}	6.0×10^{-6}	0.79	8.4×10^{-6}	7.7×10^{-6}	0.81
$J[HNO_3]$, 1/s	3.7×10^{-7}	2.8×10^{-7}	0.75	6.2×10^{-7}	5.3×10^{-7}	0.83	7.5×10^{-7}	6.5×10^{-7}	0.87
$J[HNO_2 \rightarrow OH + NO]$, 1/s	1.3×10^{-3}	0.9×10^{-3}	0.70	2.0×10^{-3}	1.6×10^{-3}	0.74	2.5×10^{-3}	2.0×10^{-3}	0.71
$J[HCHO \rightarrow H + HCO]$, 1/s	1.8×10^{-5}	1.4×10^{-5}	0.72	3.1×10^{-5}	2.7×10^{-5}	0.80	4.0×10^{-5}	3.5×10^{-5}	0.82
$J[HCHO \rightarrow H_2 + CO]$, 1/s	2.8×10^{-5}	2.1×10^{-5}	0.71	4.7×10^{-5}	3.8×10^{-5}	0.77	6.3×10^{-5}	5.0×10^{-5}	0.76
$J[CH3CHO \rightarrow CH_3 + HCO]$, 1/s	2.3×10^{-6}	2.3×10^{-6}	0.75	4.9×10^{-6}	5.3×10^{-6}	0.85	8.1×10^{-6}	8.5×10^{-6}	0.88
$J[Acetone]$, 1/s	2.9×10^{-7}	2.7×10^{-7}	0.76	6.18×10^{-7}	6.4×10^{-7}	0.86	1.0×10^{-6}	1.0×10^{-6}	0.89

[a]Observed RNO_3 here is the sum of observed 2-BuONO$_2$, 2-PeONO$_2$, 3-PeONO$_2$, n-PrONO$_2$, i-PrONO$_2$, MeONO$_2$, and EtONO$_2$ measured by *Blake and Atlas* [2003].

[b]The aerosol extinction coefficient (AOE) is the sum of aerosol absorption at 565 nm and aerosol scattering at 550 nm.

[12] Another important source of aerosols and trace gases in the springtime in Asia is biomass burning. Daily averaged CO, BC, and OC emission estimates were prepared based on the analysis of daily AVHRR fire counts as discussed by *Streets et al.* [2003a, 2003b] and *Woo et al.* [2003]. Volcanoes are one of the major sources of sulfur dioxide in Asia. Estimated volcano SO_2 emission for the major active volcanoes within the modeling domain are included in the analysis. During TRACE-P large quantities of SO_2 were emitted (as much as 10 million ton-SO_2/year) from the Miyakejima Island (Mt. Oyama) just south of Tokyo [*Yoshino et al.*, 2002]. Biogenic emissions of isoprene and monoterpenes were also included in the analysis and were based on the work of *Guenther et al.* [1995].

[13] A summary of the combustion (fossil, biofuel, and infield biomass) emissions used in the calculations is presented in Table 1. Shown are the primary emissions by region, by anthropogenic combustion (biofuel and fossil) and by open biomass burning (BB). China dominates the emissions of most species (e.g., accounting for 60% of the total SO_2 emissions). While anthropogenic sources dominate the emissions of many species (e.g., SO_2 and pentene), biomass burning is a significant source of CO, BC, ethane, and the major source of organic carbon and formaldehyde. Assessing the relative importance of biomass burning and anthropogenic emissions on the chemistry of the East Asia troposphere was a major goal of the TRACE-P experiment. The use of models in meeting this goal will be addressed later in this paper and in the work of *Tang et al.* [2003b]. The emissions data is available from the ACESS website http://www.cgrer.uiowa.edu/EMISSION_DATA/index_16.htm.

3. Results

[14] As mentioned previously, our modeling system and emission estimates were applied for the first time in support of the TRACE-P experiment. The comparison of the calculated values with observed quantities provides a test of the emissions estimates, and the transport and chemical processes represented in the model.

3.1. Mission-Wide Perspective

[15] To characterize the model's abilities and limitations, the model results are compared with the aircraft data. For these comparisons the 5-min merged data sets for the P-3B and DC-8 were used. The model was sampled every five minutes along each flight-track for the period when the aircrafts were operating in the western Pacific (4 March to 2 April 2001). Model results were interpolated to the aircraft location and time (using trilinear interpolation). Here we focus on the postanalysis results. The evaluation of the forecast results will be the subject of a future paper.

[16] A qualitative comparison of the calculated meteorological fields is shown in Figure 3. Shown are the vertical distribution of wind speed and relative humidity for all flights (DC-8 and P-3B combined). The model is able to produce the major features of the observed fields of wind speed, temperature, and pressure (not shown). Wind direc-
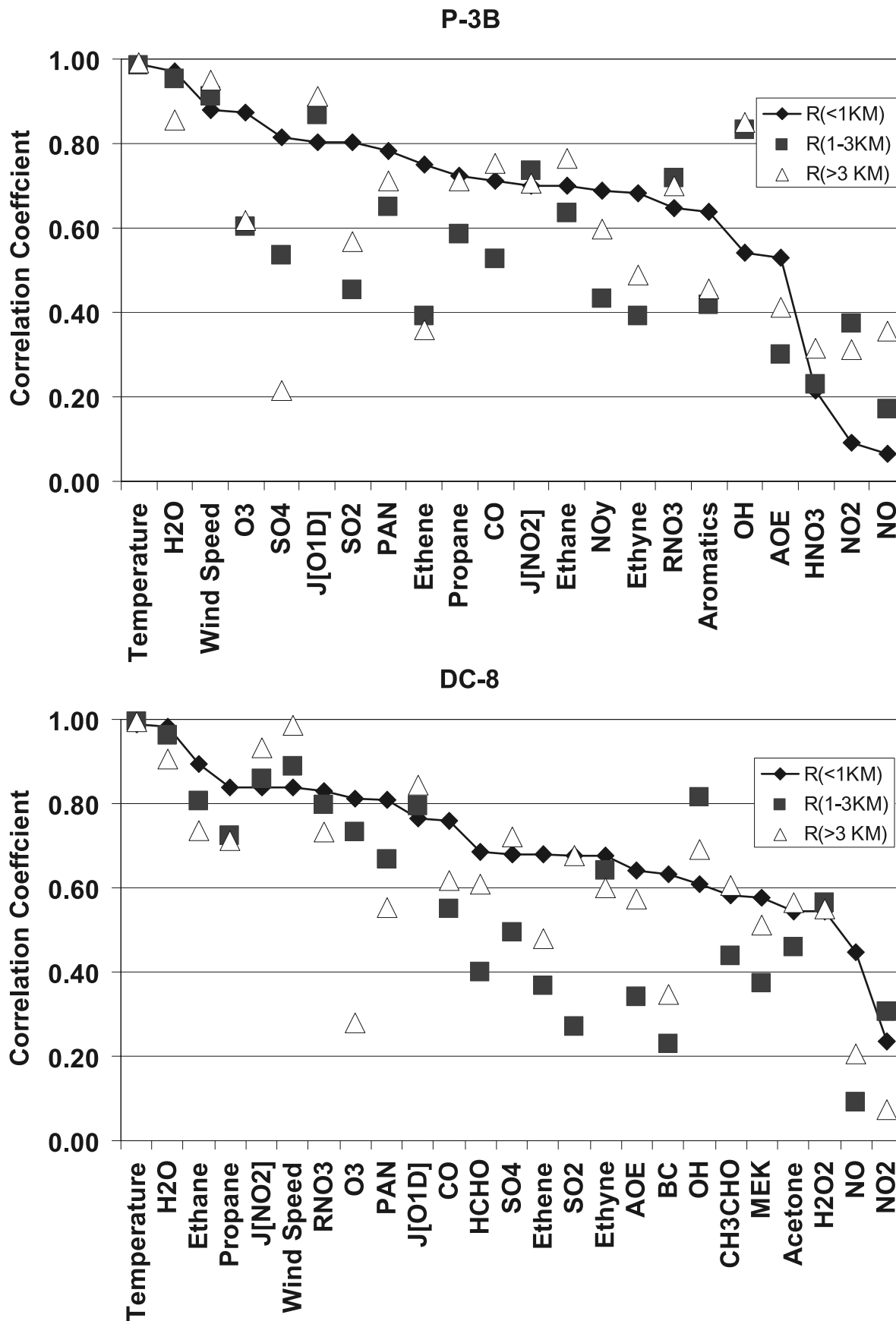
Figure 4. Correlation coefficients between observed and modeled meteorological and species parameters for the <1 km, 1–3 km, and >3 km altitude bins for the DC-8 and P-3B aircraft data.
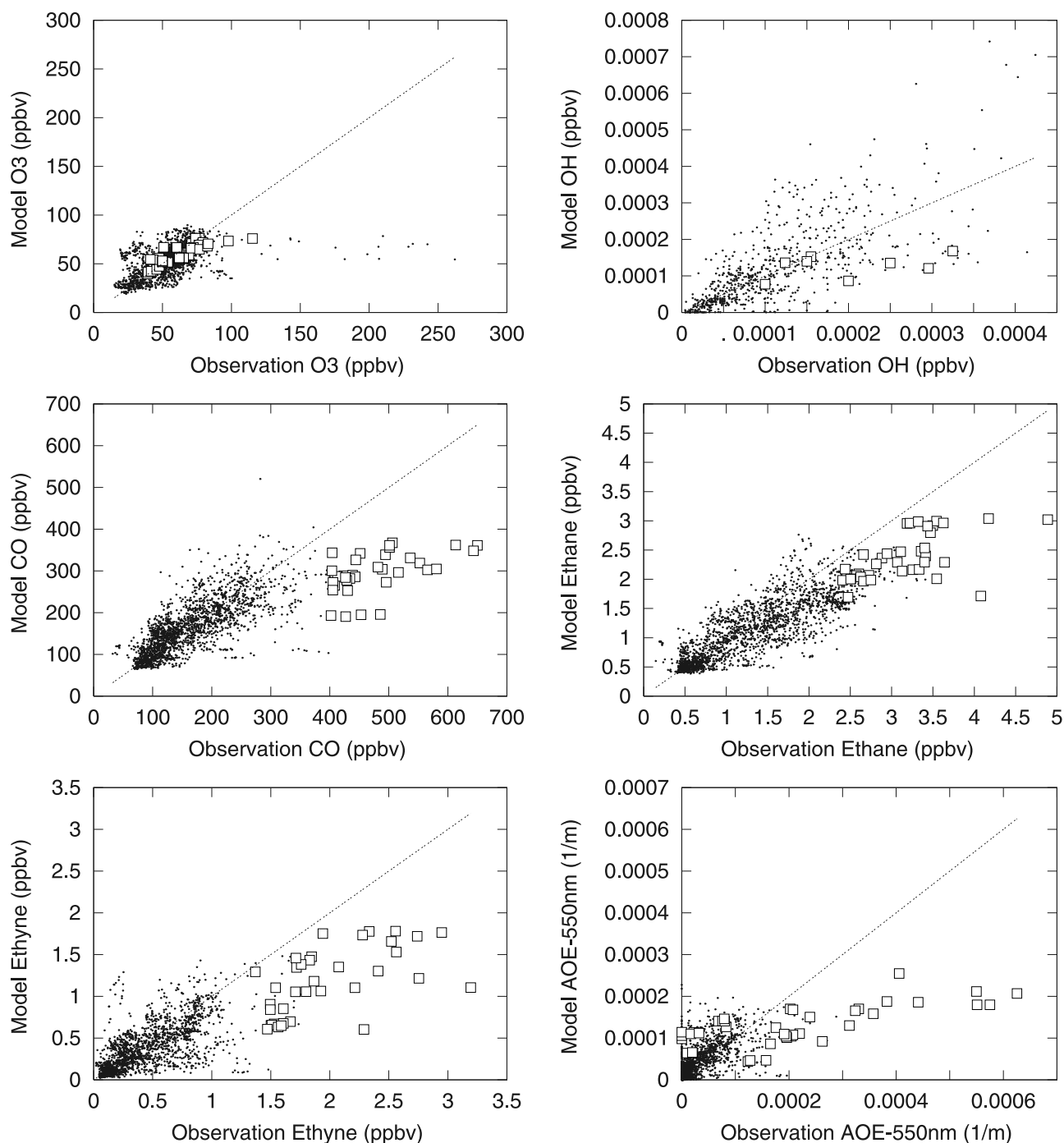
Figure 5. Comparison of measured and modeled trace gas and extinction for the DC8 and P-3B aircraft data. Shown are values for each 5-min flight segments from the merged data set. Red points indicate points where observed CO is greater than 400 ppb.

tion is more difficult to calculate accurately, especially in calm conditions (not shown). Relative humidity shows a high model bias at low relative humidity near the surface and at altitudes above 3 km. Modeled and observed ethane and ozone as a function of latitude are also shown in Figure 3. As ethane is not efficiently removed by wet processes and reacts relatively slowly in the gas phase, its distribution reflects mainly the source distribution and transport pathways. Both observed and modeled ethane show a strong latitudinal gradient, with values increasing above 25N,

consistent with the estimated emissions associated with anthropogenic activities in China, Korea, and Japan. When the data is compared point by point, we found that 80% of the model calculated ethane values fall within ±30% of the observed values and 86% of the data is captured to within a factor of 2. A persistent underprediction is shown above 40N. This is associated with flows from western Russia. Our updated emissions work did not include a reanalysis of Russian sources. Gas processing activities in this region may be underestimated in the current inventories.
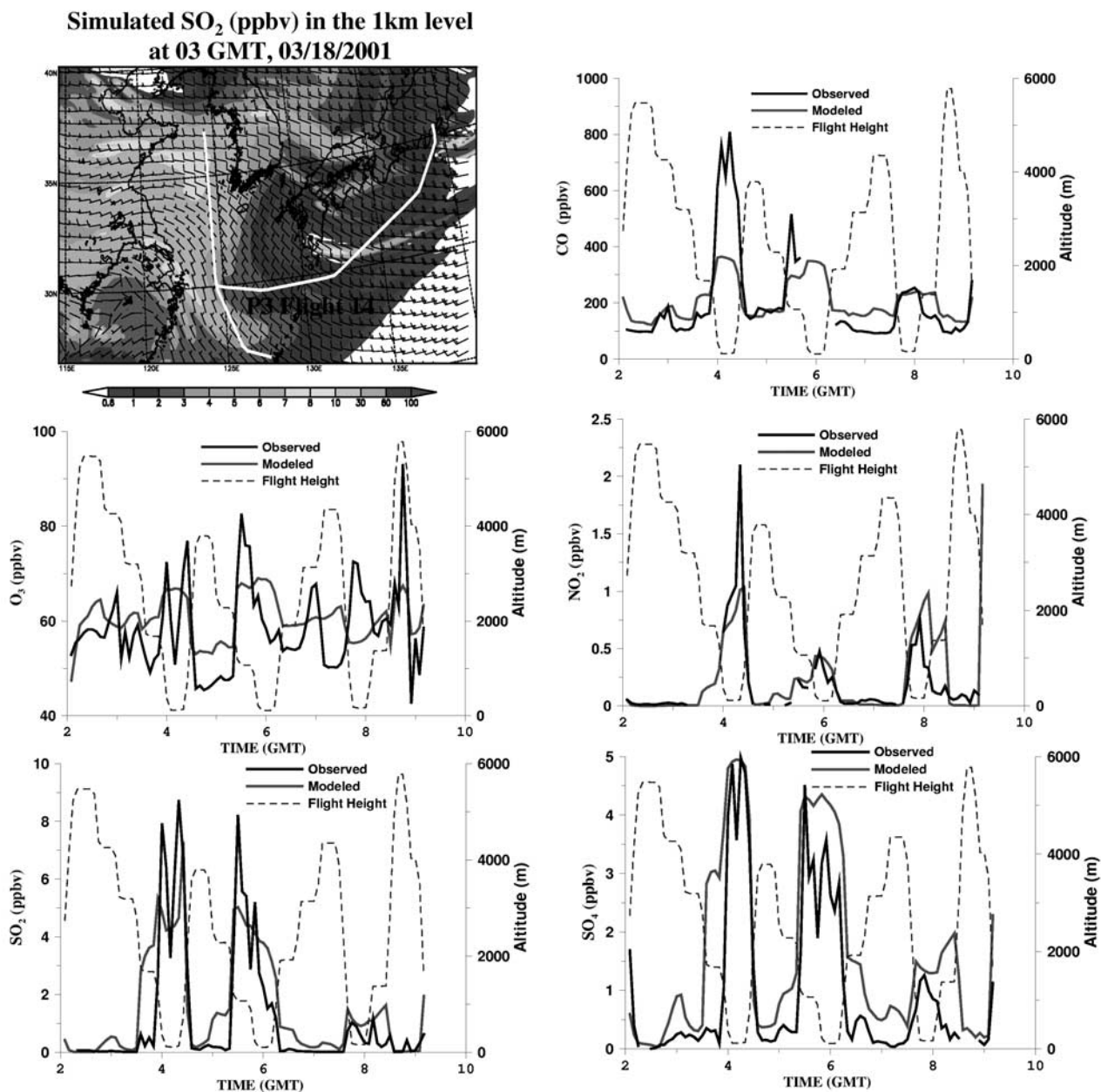
Figure 6. Comparison of observed and predicted species along the P-3B flight path on 18 March using the 5-min merged data set. See color version of this figure at back of this issue.

[17] The latitudinal distribution of ozone shows an increase in ozone with increasing latitude. The region below 10N is out of our domain and thus there are no predicted values shown. The very high values (>120 ppb) are all associated with stratospheric air that was sampled by the model on a few flights. In our analysis we set stratospheric ozone in the upper model layers according to potential vorticity (PV). Our model underestimated the impact of stratospheric ozone.

3.2. Mission-Wide Summary of All Modeled Parameters

[18] A summary of the performance of the model for each of the model-calculated parameters is presented in Tables 2

and 3 for the DC-8 and P-3B platforms, respectively. For the DC-8 data, the mean values calculated by the model are within ±30% of the observed values for all the parameters for measurements below 1 km. Above 1 km, all the modeled mean values are within ±30% with the exception of RNO_3, NO_2, C_2H_6, and SO_2 in the 1–3 km region, and SO_2, NO_2, and NO for altitudes above 3 km. Below 1 km, correlation coefficients (R) are greater than ∼0.7 for 21 of 31 parameters and exceed 0.5 for all parameters except NO_2 and NO. In general the regression coefficients decrease with increasing altitude (e.g., ethane value is 0.83 at altitudes below 1 km and 0.72 at altitudes above 3 km). But a few species have their lowest R values below 1 km (i.e., OH and HO_2). For points above 1 km, some parameters are better predicted
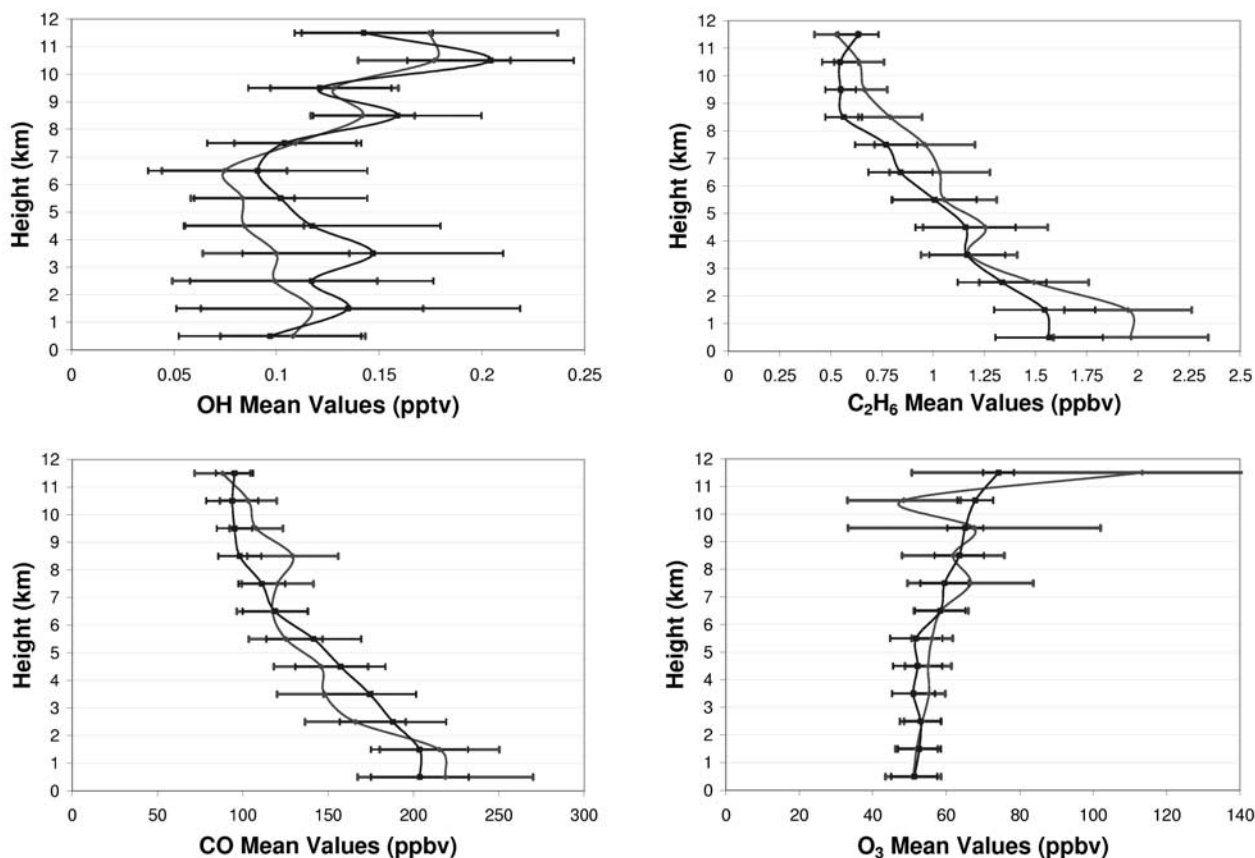
Figure 7. Comparison of the observed (red) and modeled (blue) vertical profiles of OH, C_2H_6, CO, and O_3 for the DC8 data. The horizontal bars indicate the ± one standard deviation for each 1 km altitude bin. See color version of this figure at back of this issue.

in the 1–3 km range than above (as is the case for ozone), while others have their lowest R values in the 1–3 km range (e.g., CO, SO_2, NO).

[19] Qualitatively, a similar story emerges from the comparisons with the P-3B data, although the details are different. For those parameters measured by the same groups and techniques on the two platforms (e.g., CO, O_3, ethane, propane, RNO_3, J-values) the model performance for the P-3B data is very similar to that for the DC-8, although the correlations vary slightly. Furthermore the mean values derived from the observations vary somewhat, reflecting differences in the sampling strategies (e.g., the P-3B flew lower and spent more time in the boundary layer). For example, in the case of CO the mean values in the 1, 1–3, and >3 km regions are for the DC-8 (and P-3B): 218.8(235.3); 188.3(208.1); and 122.4(136.1), respectively. The modeled values show a similar behavior with higher CO levels calculated for the P-3B.

[20] For the same parameters but measured with different techniques (e.g., SO_2, sulfate, OH, HO_2, NO, and NO_2) the differences were sometimes large. For example in the case of OH, the mean of the observed values below 1 km was 0.21 ppt on the P-3B and 0.11 ppt on the DC-8. The modeled values were also higher for the P-3B than for the DC-8, but the differences were much smaller (the modeled values were 0.11 ppt for the P-3B and 0.10 ppt for the

DC-8). There were also examples of the same parameter measured on the same platform using different techniques (e.g., acetone and acetaldehyde on the DC-8). Differences between the two measurements were observed, and the differences were present at each altitude bin. These measurements were conducted using new techniques, and were compared for the first time on the DC-8 in TRACE-P. Further intercomparison efforts are now underway focused on understanding the reasons for these differences [*Eisele et al.*, 2003].

[21] To aid the discussion of comparison of model performance by species and altitude, the correlation coefficients in Tables 2 and 3 are plotted in Figure 4. As we discuss these results it is important to keep in mind the issue of how to judge these findings. What are (or should be) our expectations of our capabilities to model ambient levels of trace species in this region? One important observation from Figure 4 is that the meteorological parameters are modeled most accurately (in terms of explaining the variance). This clearly reflects the large amount of observational data ingested into the reanalysis of the large-scale meteorological fields. However, even with this large amount of assimilated information, the differences between the mean observed and modeled water vapor concentrations away from the surface remain significant (30–40% above 3 km as shown in Tables 2 and 3).
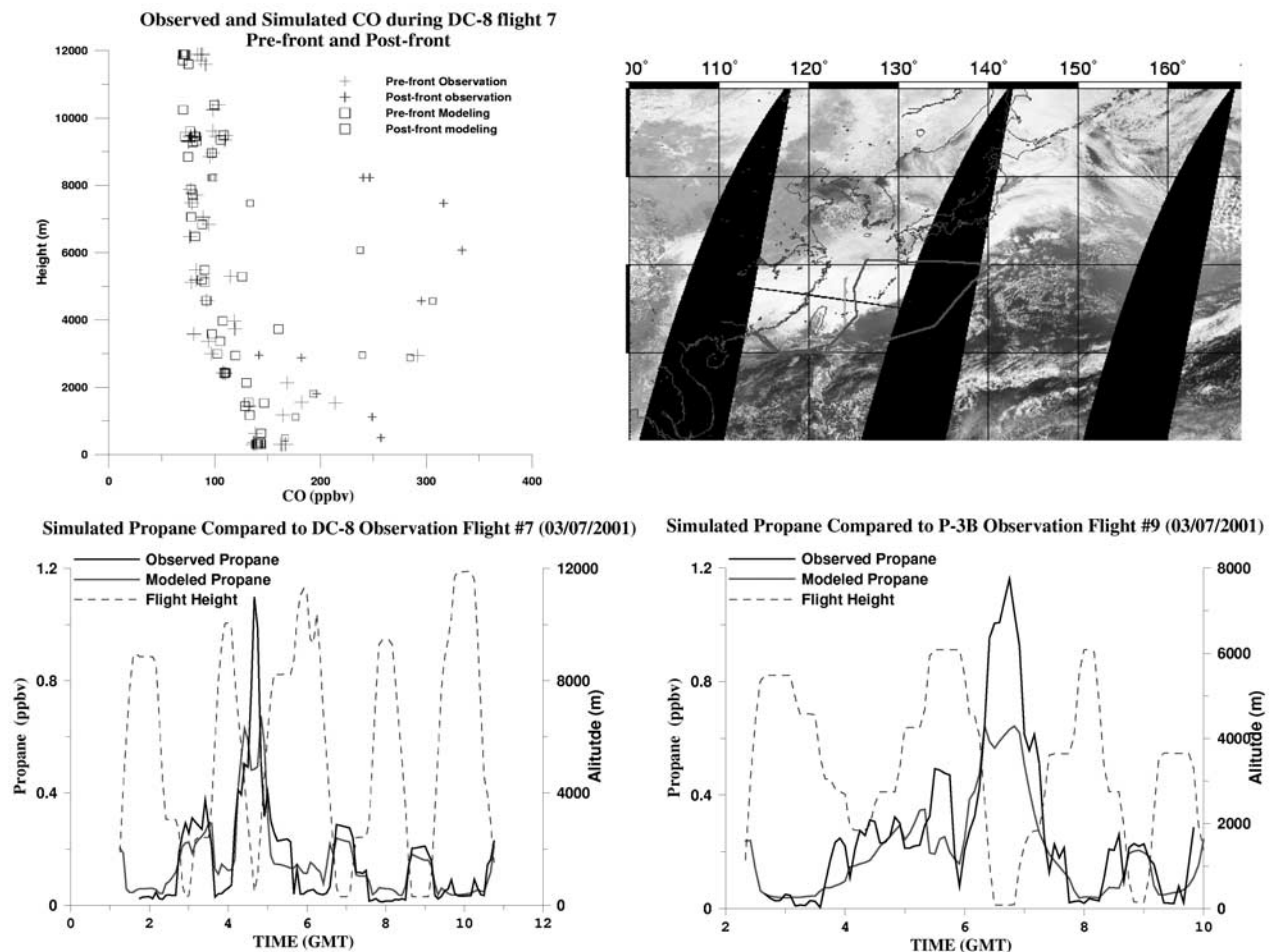
Figure 8. Observed and simulated vertical profiles of CO on DC8 flight 7 in the prefrontal and postfrontal regions. Also shown are the observed and calculated propane mixing ratios for the DC8 flight 7 and P-3B flight 9. The flight paths are also show (red is DC8; gold is P-3B). See color version of this figure at back of this issue.

[22] It can be argued that our capability to model ambient trace species should be less than that for the meteorological parameters, given that the trace gas species distributions depend on the meteorological fields themselves and that they also depend on the emission estimates, which too are highly uncertain. In the work of *Streets et al.* [2003a, 2003b] we estimate the uncertainty in the magnitude of emissions for all of Asia to be: ±16% (SO2), ±37% (NOx), ±130% (NMVOC), ±185% (CO), and ±360% (BC). Further complicating our ability to predict trace species is the nonlinearity and species interdependencies introduced by the photochemical oxidant cycle and the fact that observational data on the chemical constituents are not assimilated into the analysis.

[23] What we observe is that the correlation coefficients for the trace species are lower than those for the meteorological parameters. To focus the discussion we restrict our comments here to the lowest 1 km. For some species distributions that are controlled by transport and emissions processes (e.g., ethane and propane), correlations are high (0.89 and 0.84, respectively, for the DC-8 data). However, CO and ethyne also have simple removal mechanisms in the atmosphere, yet they have lower R values (0.76 and 0.68,

respectively). This reflects the fact that the emissions of CO and ethyne arise from all types of combustion processes, many of which are highly uncertain in magnitude and/or in spatial/temporal distribution (e.g., biomass burning, domestic cooking, and heating).

[24] The species with the least uncertainty in the emissions is SO_2. However, the distribution of SO_2 and its oxidation product, sulfate, are determined by the SO_2 source distribution, by transport, by chemical processes in both gas and liquid phases, and by wet and dry deposition processes. Thus the sulfur atmospheric cycle is more complex than that for CO (in terms of breadth of processes). The model performance for these species falls between those for ethane and ethyne.

[25] The correlation coefficients for the main photochemical products, O_3 and PAN, are larger than 0.78. The distributions of these species depend on transport processes, as well as photochemical processes involving NO_x and VOC precursors. The TRACE-P experiment measured many important components of the photochemical oxidant cycle that can be used to evaluate how well the model captures the photochemical cycle. After NO_x is emitted into the atmosphere it becomes partitioned into many different
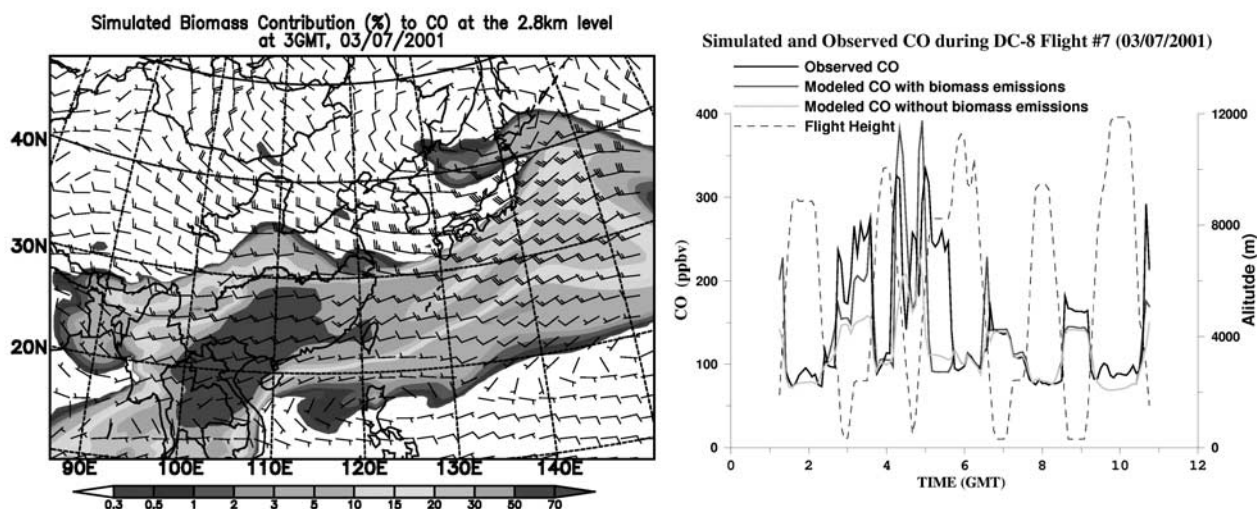
Figure 9. Observed and calculated CO for DC8 flight 7. Shown are results with and without biomass burning emissions. The contribution of CO (expressed as fraction) due to biomass burning obtained by runs with and without the biomass burning sources at 2.8 km is also shown. The flight path is shown in Figure 8. See color version of this figure at back of this issue.

forms as the result of the photochemical oxidant cycle. Measurements of NO_y provide an integrated measure of how much of the NO_x emitted remains in the atmosphere. The R value for NO_y is ~0.7, slightly lower than that for ozone. However, when we look at the individual components of NO_y we find discrepancies. For example, in terms of NO and NO_2 the model captures the magnitudes accurately (in the mean) but produces the lowest R values of any parameter (0.45 and 0.24, respectively, for the DC-8 data). This reflects in part the fact that in the TRACE-P experiment we observed aged air masses with most of the emitted NO_x converted to other forms by the time that the air masses were sampled by the aircrafts. Nitric acid is a main product of NO_x oxidation in the atmosphere. The correlation coefficient for HNO_3 is higher than those for NO and NO_2, but its magnitude is overestimated at low altitudes. Our analysis has not yet included a detailed treatment of heterogeneous reactions on aerosol surfaces. We expect that the heterogeneous removal of nitric acid associated with aerosol-rich air masses in east Asia is an important sink mechanism that will result in a lowering of ambient nitric acid levels [*Song and Carmichael*, 2001; *Underwood et al.*, 2001]. This will be the subject of a future paper.

[26] The model performance related to some of the important reactive hydrocarbon species was discussed already. There are many reactive hydrocarbon species in the atmosphere. Formaldehyde represents a particularly important species in this regard, as it is both a primary pollutant and a product of oxidation of a wide variety of reactive hydrocarbons. Analysis of the model performance for formaldehyde provides an integrated assessment of how ell the model and emissions are representing total reactive hydrocarbons. Formaldehyde is modeled with a skill similar to that for CO and SO_2 (R = ~0.7).

[27] Another key component to the analysis of the photochemical oxidant cycle is the photolysis rates. Photolysis rates depend on many factors including the influence of clouds and aerosols. In our analysis photolysis rates (i.e., J-values) are calculated based on modeled cloud and aerosol quantities, and are predicted with similar skill as CO and ozone. Finally a key measure of the local photochemical oxidation state of an air mass is provided by the concentrations of the OH and HO_2 radicals. Their levels in an air mass depend on many of the ambient parameters discussed above (NO_x, water vapor, ozone, hydrocarbons, photolysis rates, etc.), and their values adjust themselves very quickly to changes in these parameters. Our model captures the mean distributions accurately (within 10%), and with R values greater than 0.6.

3.3. Sources of Discrepancy

[28] The results presented in the last section give an overall summary of the model's capabilities to predict trace species distributions. We showed that the model can at best explain ~65% of the variability seen in the observations (as measured by R^2). So it is important to isolate specific conditions under which the model has particular deficiencies and relate these to problems in processes or emissions.

3.3.1. Yellow Sea

[29] Further insights into conditions where the model deviated significantly from the observations are obtained by examining the scatterplots of modeled versus observed quantities, and looking for similarities between species. Sample results for all flights are presented in Figure 5. From these comparisons we see that there is a tendency for the model to underpredict CO at high-observed CO values. The points marked in red in the CO plot represent observations with CO > 400 ppb. The corresponding concentrations of other species for these high-CO observations are depicted in the other frames. At the same points where we underestimate CO, we tend to underestimate extinction and ethyne but predict OH and ozone with no apparent biases. Results from trajectory analysis (not shown) found that all of these underestimated CO points were associated with low
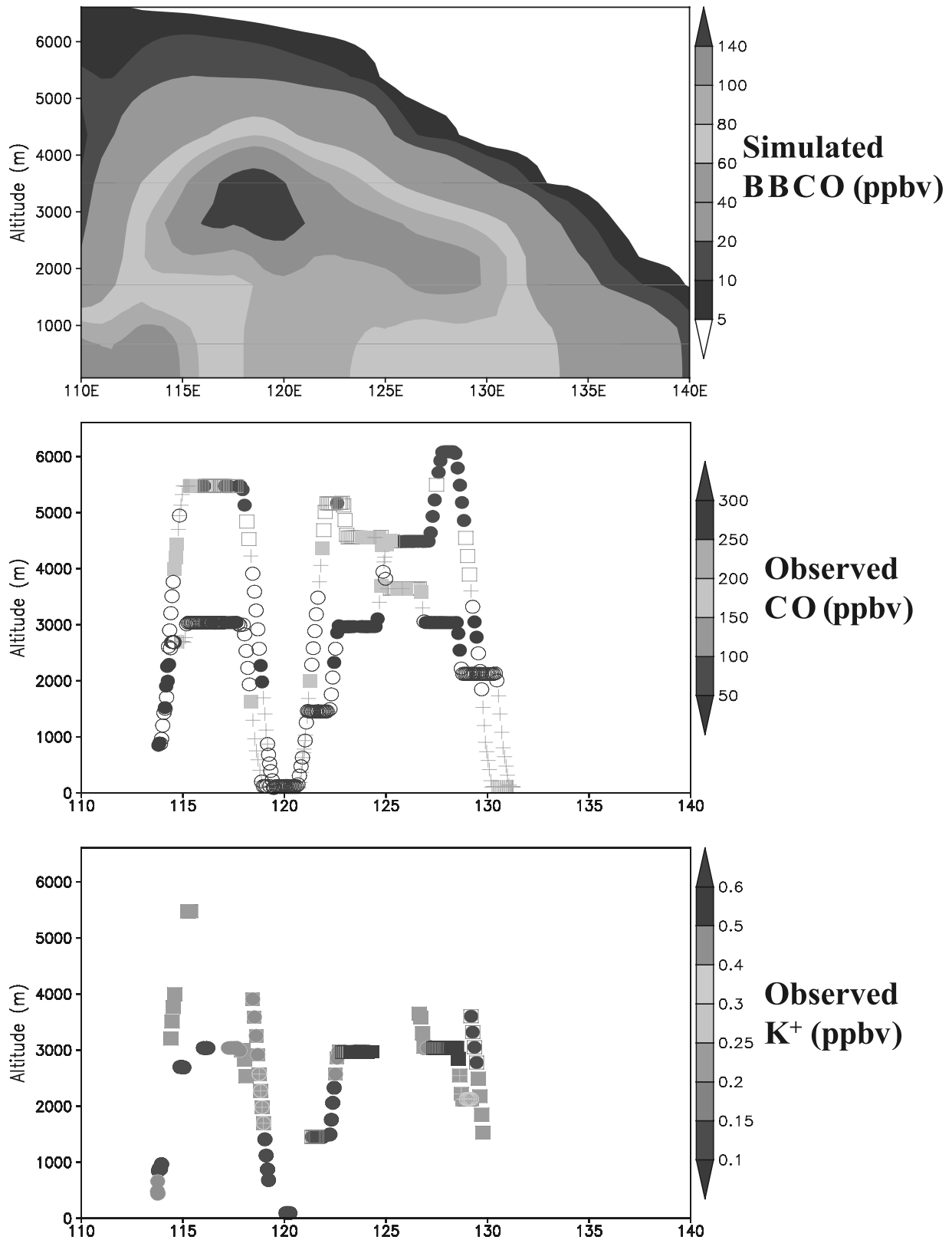
Figure 10. Forecast of CO due to biomass burning along 20N at 3 GMT (12 Japan Standard Time (JST)) on 9 March (top). Shown is the vertical distribution of primary CO due to biomass burning. The observed total CO and aerosol potassium measured by G. Sacshe and R. Weber, respectively, are also shown. Potassium provides a good tracer for biomass burning. See color version of this figure at back of this issue.
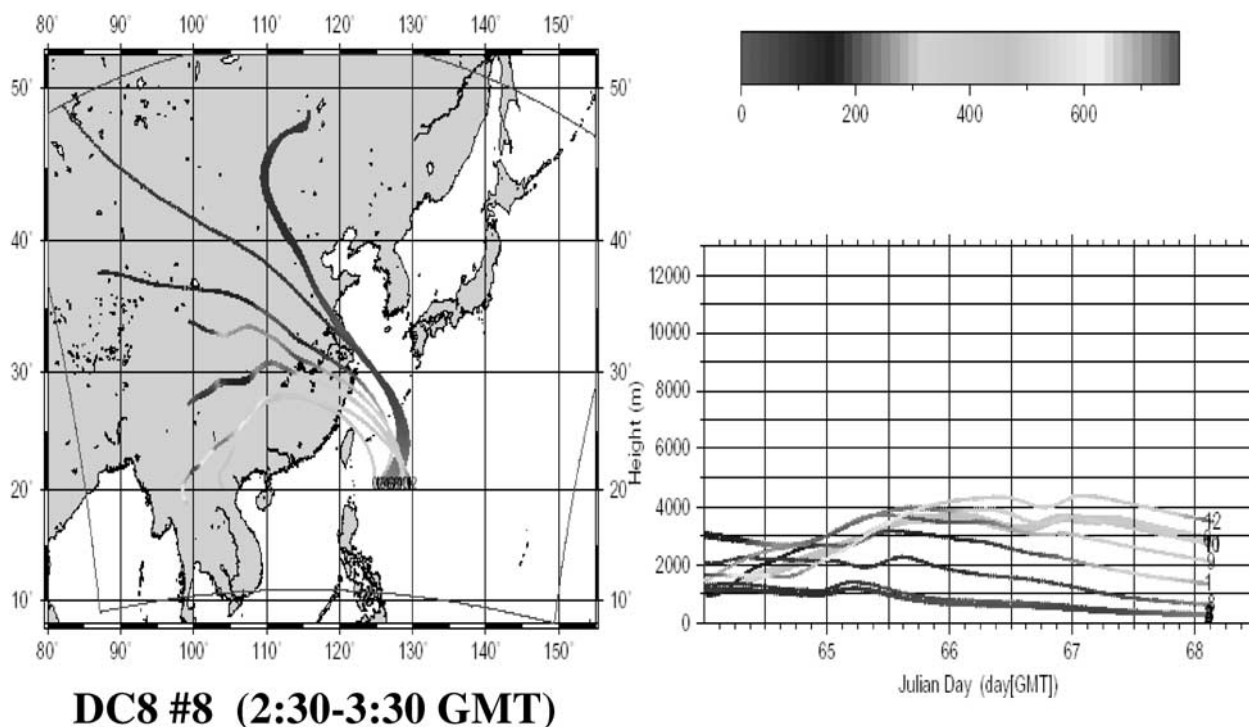
Figure 11. Five-day back trajectories every five minutes along the DC8 flight path from 2:30–3:30 GMT for flight 8. Trajectories are colored by modeled CO. See color version of this figure at back of this issue.

altitude observations in the Yellow Sea, with back-trajectories that passed over Shanghai and surrounding areas.

[30] Many TRACE-P flights operated in the Yellow Sea to look at outflow downwind of the high source regions in eastern China. One such experiment was the P-3B flight 14 conducted on 18 March 2001. On 17 March a developing wave cyclone was located east of Shanghai and an anticyclone was centered just east of Tokyo. The wave cyclone intensified during the day and moved eastward, and its associated cold front also swept towards the east. On 18 March the wave cyclone was located just off the northeast coast of Japan; and was moving towards the northeast. Pollutants were transported off the cost of China at low altitudes and towards Japan as this front swept to the east.

[31] The flight path of the P-3B and observed and measured values are presented in Figure 6. Elevated levels of pollutants were found at multiple levels between the surface and $\sim$2 km throughout the flight path in the Yellow Sea. The model values show these features, and a wide variety of calculated primary and secondary species agree well with the measured values. As discussed above, the model consistently underpredicted CO at low altitudes in the Yellow Sea, and this is clearly shown in the low altitude leg at $\sim$4 GMT. The model places this plume at the right location but underestimates the value. A similar finding holds for SO_2 and NO_2. Ozone at this time is elevated, but while the model shows a broad maximum, the observations show a more distinct plume, with a local ozone minimum coincident with the local peak in NO_2. In fact a close inspection of the observed CO and SO_2 features at this time (and again between 5 and 6 GMT) shows two distinct peaks, one located near the surface and the second elevated

layer between 1 and 2 km. These results show that there are fine-scale structures, associated with plumes that are not resolved by the model using an 80 km horizontal resolution.

[32] *Tu et al.* [2003], using their fast time resolution (>1 Hz) SO_2 measurements, investigated how clouds impact the dynamics of the lower atmosphere and effect transport in the 1–3 km layer over marine surfaces. In that paper a comparison of their observations with our model results were made for the flight discussed above, as a well as the same flight plan executed on the previous day (i.e., 17 March). The transport patterns for these 2 days were very similar; however the flight on the 17th encountered low-level stratus clouds, while the flight on the 18th was under clear skies. They observed for both cases a high degree of vertical structure in the SO_2 between the surface and 3 km. When compared to our model results, the model performed better for the cloud-free case, but even under this case the model over-predicted SO_2 levels in the 2 km layer. The fine structure in observed SO_2 was correlated with the fine-scale vertical structure in the turbulence fields. This fine-scale turbulence structure was not adequately resolved in our present modeling analysis. A more detailed treatment of the dynamics in the continental/marine transition region, and finer vertical resolution in the CFORS meteorological analysis, are required to more accurately capture this behavior. This line of study is now underway.

3.3.2. Vertical Profiles

[33] As discussed in section 3.2, the model performance varied significantly with altitude. Additional insights into the model performance as a function of height can be seen in comparing vertical profiles. The calculated and observed vertical profiles for OH, CO, C_2H_6, and O_3 for the DC-8
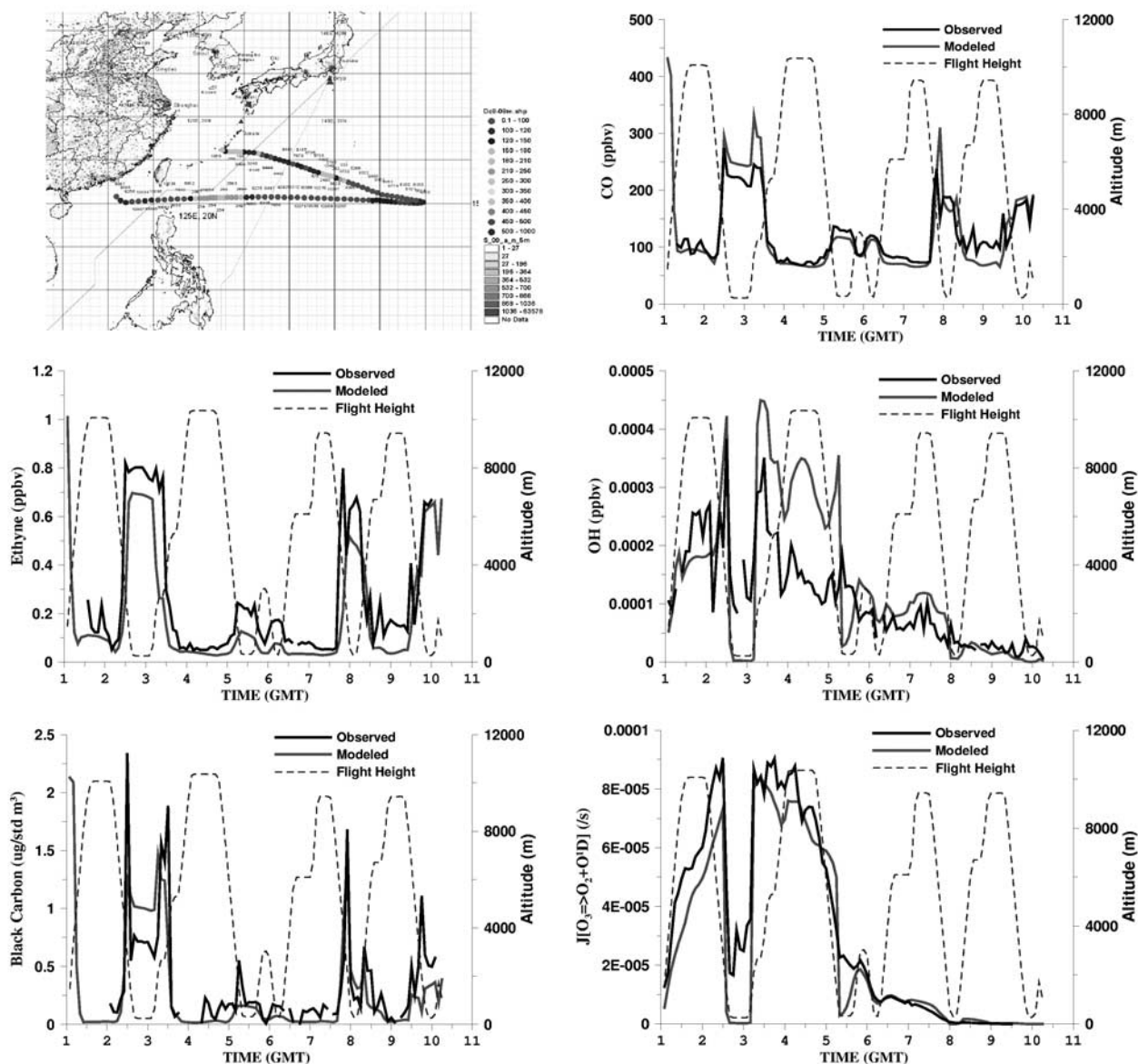
Figure 12. Comparison of observed and predicted species along the DC8 flight 7 path on 9 March using the 5-min merged data set. See color version of this figure at back of this issue.

values are presented in Figure 7. To evaluate more completely the model performance, we binned the observed and predicted values into 1 km layers and then performed a linear regression analysis that also tested the statistical significance of the relationship. The vertical profiles are plotted as the mean value of each 1-km bin, and the bars indicate ± one-standard deviation. The predicted and model behavior were determined to show a significant linear effect (significant linear correlation at 95% confidence) for all vertical layers except 11 and 12, for the species shown. As also shown, both the observed and predicted values show a large standard deviation at each layer.

[34] CO and C_2H_6 have long lifetimes in the atmosphere, and their vertical distribution is determined by emissions and transport processes. CO and C_2H_6 show enhanced values in the boundary layer, at 3–5 km, and at 6–9 km. The large variation in magnitude in the lowest 1km reflects

the large contrast between the clean marine air and the strong plume-like features observed in postfrontal outflow in the Yellow Sea, as shown in Figures 5 and 6, and discussed above. The features at 3–5 km are associated with outflow in the warm conveyor belt region (as illustrated in Figure 2), while features at 6–9 km are associated either with deep convection within East Asia, or long range transport from extra-Asia regions (as discussed by *Jacob et al.* [2003]). The model profiles tend to be smoother than observed and are low at low altitudes, high at middle altitudes, and low at high altitudes. This suggests that the cloud transport processes in the model may be too diffusive. Model errors associated with where and when the air mass is lifted and errors associated with the location and timing of biomass emissions can result in a displacement of the vented air mass away from where it was observed. *Kiley et al.* [2003] intercompared calculated CO fields from seven
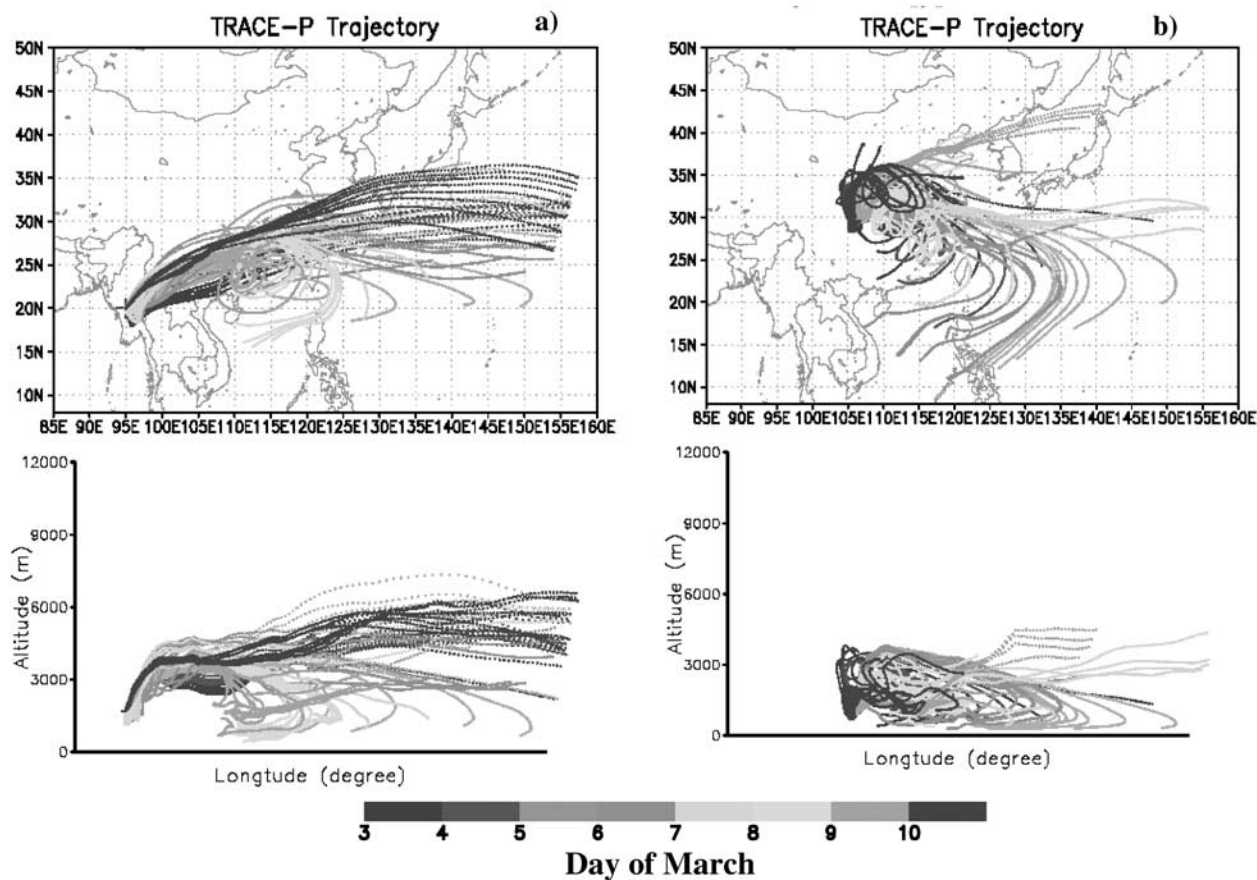
Figure 13.   Five-day forward trajectories from a biomass source region in SE Asia (a), Chongqing (b), Shanghai (c), and Qingdao (d). See color version of this figure at back of this issue.

CTMs used during TRACE-P and found that the most significant differences between all the models and the observations occurred in outflow regions, above 4 km.

[35] The vertical profile of OH is markedly different than those for primary species such as CO and ethane, with a local minimum at $\sim$7 km and a general increase with height above this layer. OH also shows a large standard deviation at each height. These facts reflect the dependency of OH on water vapor, sunlight, and ozone. A further consideration in comparing the OH profiles is that the measurements of OH from aircraft remains difficult and the measurement errors are significant (estimated at $\pm$ $\sim$25%). With this consideration, the predicted OH values are well within the measurement errors. Ozone shows an increase with height. The observations show a large standard deviation above 8 km, indicating the occasional observation of air of stratospheric origin. The model treatment of stratospheric ozone scaled to potential vorticity was not able to reproduce these high values accurately.

3.4. Context Analysis of Frontal Outflow

[36] Characterizing the role of biomass burning and the role of frontal processes in determining the composition, location, and fluxes of trace gases and aerosols in the Asian outflow were important objectives of TRACE-P. Many flights were devoted to these topics. As discussed previously, pollution transport in frontal events is complex (see Figure 2). To better understand how the modeling analysis

can provide context and aid in the interpretation of the observations, we will focus here on the detailed analysis of the 7–10 March time period.

[37] During this period the DC-8 and P-3B sampled pollution outflow as a cold front swept over East Asia. The general situation of pollution transport associated with this frontal passage is shown in the bottom panels of Figure 2. The evolution of this front began on 4 March as shown in the left panel of the middle row, and intensified over the next 2 days. By 7 March (middle row, right), the low-pressure system had moved over the Japan Sea and biomass burning impacted air is transported in the warm conveyor belt, as depicted by the red plume. By 9 March, the front had begun to decay, and pollution from East Asia is being transported at low altitudes in the post-frontal region as shown in the bottom row, middle panel. TRACE-P sampled this frontal event at different stages of is evolution on 7, 9, and 10 March.

[38] On 7 March, the P-3B and DC-8 flew flight paths shown in Figure 8. The observed and modeled propane distributions along the flight path show clearly outflow within the front extending to altitudes of $\sim$6–8 km. The DC-8 was able to fly through the front and sample prefrontal air. The comparisons of the vertical profiles of CO in the prefrontal and postfrontal regions are also shown. The profiles in the prefrontal and postfrontal regions are markedly different. In the prefrontal region, CO is maximum in the marine boundary layer and
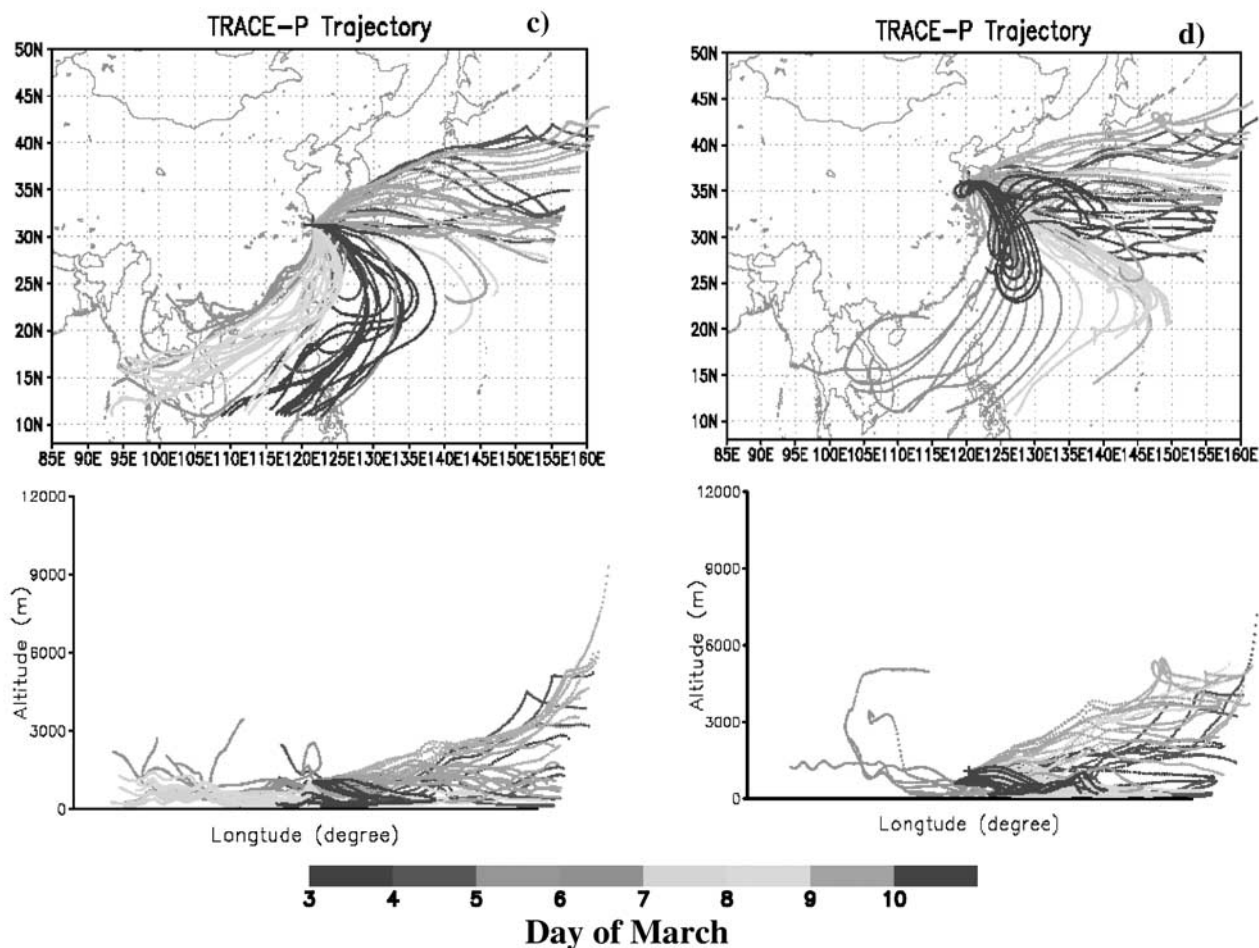
Figure 13. (continued)

decreases to ~80 ppb in the middle troposphere. In the postfrontal region there is an enhancement of CO (~200 ppb) throughout the troposphere associated with vertical lifting associated with the frontal activities. The model captures this enhancement, but underestimates the magnitude above 4 km. Simulations with and without biomass burning were performed to help identify the source of this elevated CO. Results shown in Figure 9 illustrate that CO in the layers above 2.8 km was due to biomass burning in SE Asia and transported in the warm-conveyor belt associated with this cold front.

[39] The forecasts for 9 March suggested that the location of this decaying front would be located along 20N and that air influenced by biomass emissions from Southeast Asia would be found in the warm conveyor belt of this system in a layer between 2 and 4 km. Air below this layer was predicted to contain pollution emitted around and north of Shanghai. On this day both the DC-8 and P-3B flew missions with flight paths along 20N.

[40] The forecasted biomass-burning tracer (CO) along 20N is presented in Figure 10. The forecast placed the center of two biomass plumes along 20N at these times; one between 115 and 120E; and the second between 125 and 133E. Also shown in Figure 10 are the observed CO distribution and the observed soluble aerosol K^+ concentrations (potassium is a good tracer of biomass burning)

measured on the P-3B. Observed layers of enhanced K^+ and CO are found in the warm sector outflow at the latitude and altitudes forecasted. (The warm sector is shown by the red plume structure in Figure 2 (bottom-middle). The observations also observed an elevated layer of CO and K^+ between 123 and 124E, which was not attributed to biomass burning in the forecasted fields. In the model calculation of total CO, this feature was identified, and it was a combination of biomass burning CO and CO from biofuel combustion in Southeast China. Biofuel combustion also results in K^+ emissions. To illustrate the flow patterns along the flight path, three-dimensional back trajectories for each 5-minute flight segment between 2:30 and 3:30 GMT, color coded with calculated total CO levels along the trajectory, are shown in Figure 11. These results indicate that the air sampled above ~2 km was influenced by biomass burning emissions approximately 4 days previously and that this air was lifted by orographic forcing over the highlands of northern Southeast Asia to nearly 4 km and then descended to 2−3 km in the leading edge of the surface high pressure system centered of Vietnam (see Figure 2, bottom-middle). In contrast air below 2 km passed at low altitude over the source regions of eastern China and traveled south in the low-level winter monsoon flow.

[41] Further details are presented in Figure 12, where the flight path of the DC-8, along with a sampling of the
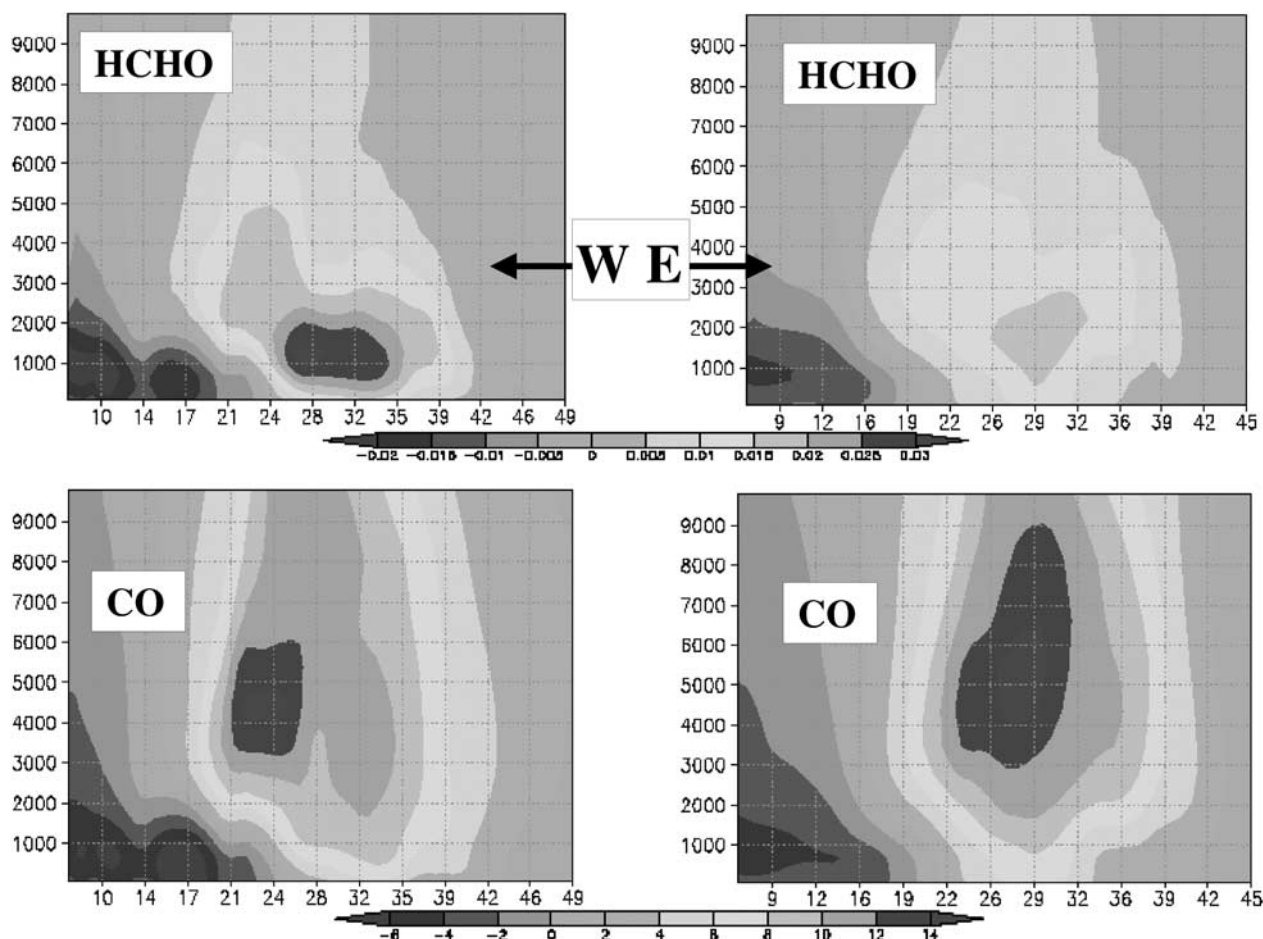
Figure 14. Calculated vertical profiles of horizontal fluxes for HCHO and CO (unit mmol/m^2/s) along the surfaces indicated averaged over 1–14 March. The west boundary is approximately 125E, the east boundary is ~145E. See color version of this figure at back of this issue.

observed and modeled distributions are shown. All the species showed a significant amount of vertical structure along the flight path. The DC-8 was able to fly sufficiently far to the east to penetrate into prefrontal air (at ~5 GMT). Primary species such as CO and BC showed concentrations in the prefrontal region to be ~1/3 of those in the postfrontal air. In the postfrontal region, CO and BC showed peak concentrations at 2–4 km but with elevated levels extending to the surface. In contrast, ethane and NO$_2$ showed enhanced levels from the surface to ~4 km but with peak values in the boundary layer. The model results clearly captured these features. In fact the model did an excellent job in quantitatively capturing many of these import features, including the location and magnitude of the peaks, the postfrontal enhancements, and the vertical variability.

[42] Calculated OH values are also shown. In many sections of the flight, modeled OH closely tracked the observed values. However, in the period of 2.5 to 5 GMT, OH in the model decreased in the boundary layer, as did the observations, but the model values went significantly lower. As the DC-8 climbed out of the boundary, both the observed and modeled values increased. In the period between 4 and 5 GMT, when the aircraft was at ~10 km, the model

significantly overpredicted OH levels. To help understand these differences between observed and modeled OH, the observed and modeled J[O^{1}D] values are also presented. The predicted values are too low in the boundary layer around 2.5 GMT, due to an overestimation of the attenuation by the calculated aerosol and cloud distributions. However, the calculated J-values at the high-altitude leg are accurately captured. We also compared the observed and calculated water vapor concentrations and cloud liquid water, and they were accurately predicted. However, the model overestimates ozone levels in the 4–5 GMT period by ~20 ppb, which in the model is due to ozone of stratospheric origin.

[43] To further illustrate how pollutants are transported during frontal passages in East Asia, we calculated three-dimensional forward trajectories from different source regions. Trajectories were initiated every 3 hours over a biomass-burning region in SE Asia, and over major emitting cities of Chongqing, Shanghai, and Qingdao over the period 3–10 March. Each trajectory was followed for 5 days. The results are shown in Figure 13. (It is important to note the limitations and uncertainties in the calculated trajectories in frontal regions and near convection. However, these trajectories often did not encounter the front until late in their
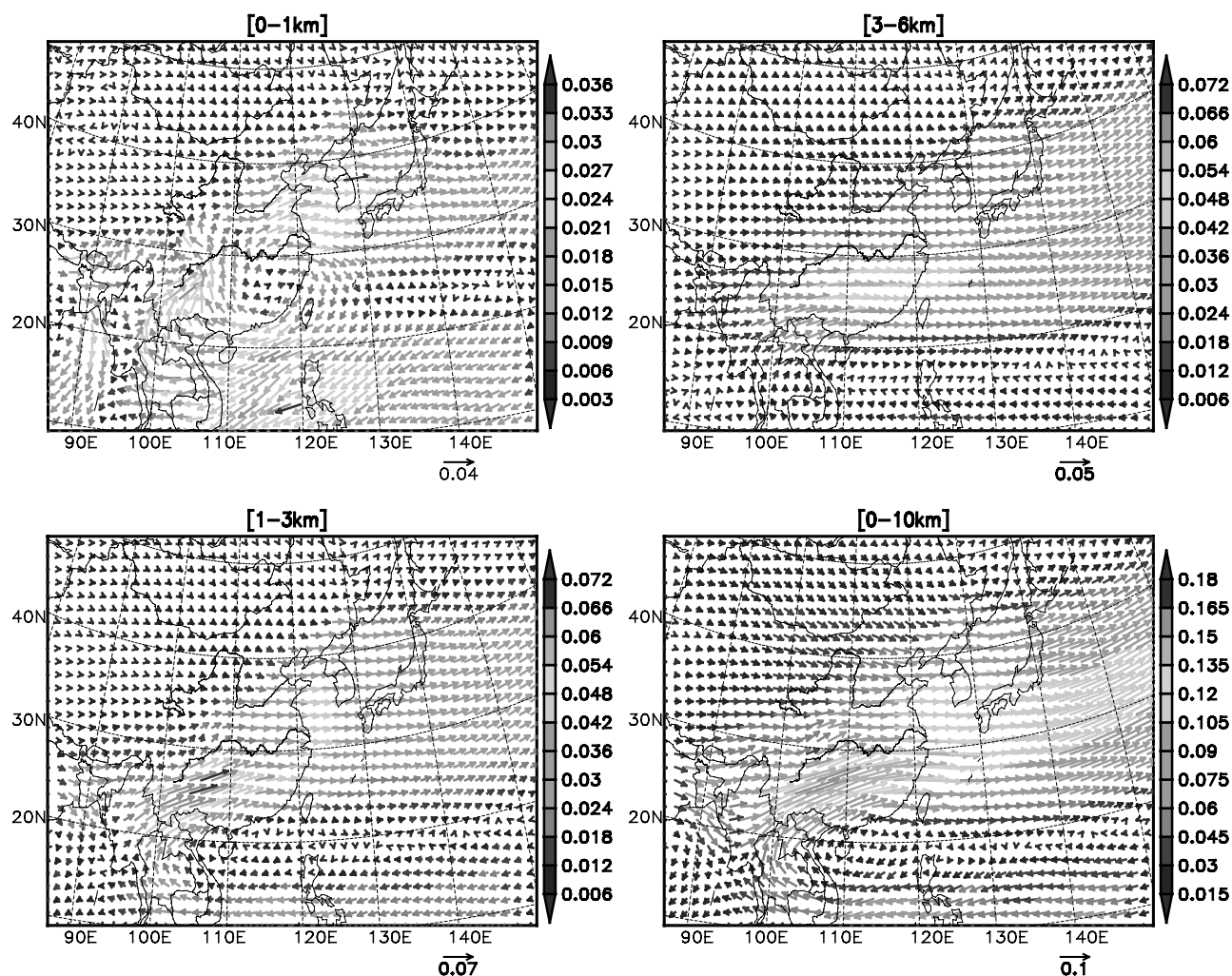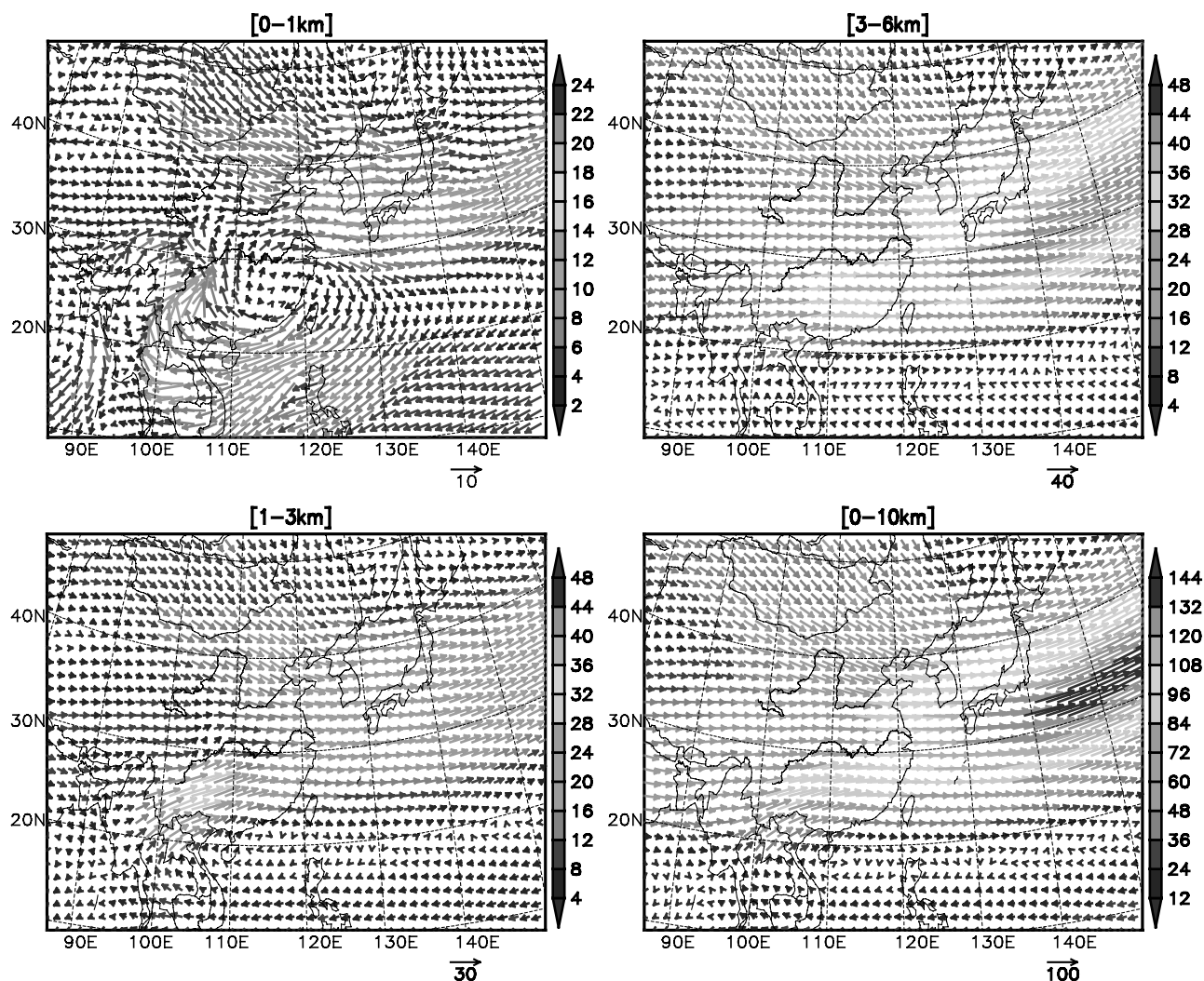
Figure 15. Calculated horizontal fluxes of HCHO (unit mol/m/s) that is vertically integrated for different vertical layers, averaged over 1–14 March. Vector indicates the flux direction. Both color and length of vector represent magnitude. See color version of this figure at back of this issue.

forward path.) For biomass burning emissions over Myanmar, we see that during this period all the forward trajectories initiated at 1 km over the source region lead to outflow into the western Pacific at altitudes between 3 and 6 km. The air masses are lifted by orographic effects associated with the mountains in northern Laos, Vietnam and southern China and aided by convection.

[44] Chongqing is a heavily polluted region located in a basin just east of the Tibet plateau. Outflow from this region is complex, and restricted to easterly outflows as transport to the west is blocked. The transport out of this region is very intermittent, with trajectories remaining over Central China for periods of days between frontal events and being transported to latitudes below 30N during postfrontal periods. Emissions from the coastal cities of Shanghai and Qingdao experience northerly, easterly, and ascending transport with the approach of the low-pressure system and southerly low altitude transport associated with trailing high-pressure systems. In these winter monsoon flows, we see that the latitudinal gradient in emissions is transformed into a longitudinal gradient at lower latitudes. For example the flights at low altitude on 9 March at 20N

were sampling air of different age and from different source regions. Air from Shanghai was expected to be found at lower longitudes, while emissions from Qingdao were expected to be located farther to the east. We also see that air from northern China can affect pollution levels over southern China.

[45] Calculated fluxes during the period 1–14 March are presented in Figures 14, 15, and 16. The vertical distributions (Figure 14) show clearly the major outflow regions. In the case of CO the major outflow conditions along ~125E show two distinct flux regions, one at lower latitudes associated with biomass burning and the second at higher latitudes heavily influenced by fuel combustion sources. The major outflow occurs between 3 and 6 km and rises to 3–8 km along the eastern boundary, associated with lifting within the frontal system as the air masses move into the western Pacific. Similar features are seen for HCHO, but the absolute flux decreases at the eastern boundary, reflecting the chemical destruction of HCHO. Further details are found in the horizontal flux plots (Figures 15 and 16). The low altitude fluxes reflect the major source areas, and the split in the transport patterns between those sources

Figure 16. Calculated horizontal fluxes of CO (unit mol/m/s) that is vertically integrated for different vertical layers, averaged over 1–14 March. Vector indicates the flux direction. Both color and length of vector represent magnitude. See color version of this figure at back of this issue.

above 30N and those below. It is interesting to note the high flux region in and around Hainan Island (110E, 19N), which represents a convergence zone where pollutants emitted from northern China and transported in the monsoon flow are brought together with the outflow of fresh emissions from south China.

3.5. Mission Averaged Distributions and Possible Biases Caused by Sampling Strategies

[46] The observations can be used to derive mission-averaged distributions. This was done by binning the observed data to a spatial (horizontal and vertical) grid and averaging all the observed values that fall within the individual bins. Mission-averaged observed fields of ethane averaged over the lowest 2 km and over the entire depth of the troposphere are shown in Figure 17. Modeled derived fields (0–2 km) sampled and averaged the same way as the observations are also shown. Comparisons of the observed and modeled fields provide a comparison of the model predictions; the fields are qualitatively similar. What the model can provide, which the aircraft can not, is an estimate

of what the mean distributions would be (in the model world) if every grid cell was sampled equally and at all times (0800 to 1700 local time) throughout the period of the TRACE-P operation (we will refer to this as "perfect sampling"). Put another way, the field experiments deploy limited resources with a prioritized list of objectives. As a result the western Pacific is not sampled randomly, but is biased towards the mission objectives (e.g., frontal outflow in biomass plume regions and downwind of megacities, etc.). The monthly mean distribution for modeled ethane based on perfect sampling is also presented. Clear differences are seen between the monthly mean and the mission-averaged ethane values in the Yellow Sea. This reflects the fact that the aircraft missions often sampled post-frontal outflow in this region. These events have the highest concentrations but occur with synoptic frequency.

[47] To quantify these results, we divided the domain into six different regions (shown in Figure 17) and computed the mean vertical profiles based on the observations, the model sampled the same as the aircraft observations, and for perfect sampling in the model. Select profiles are shown
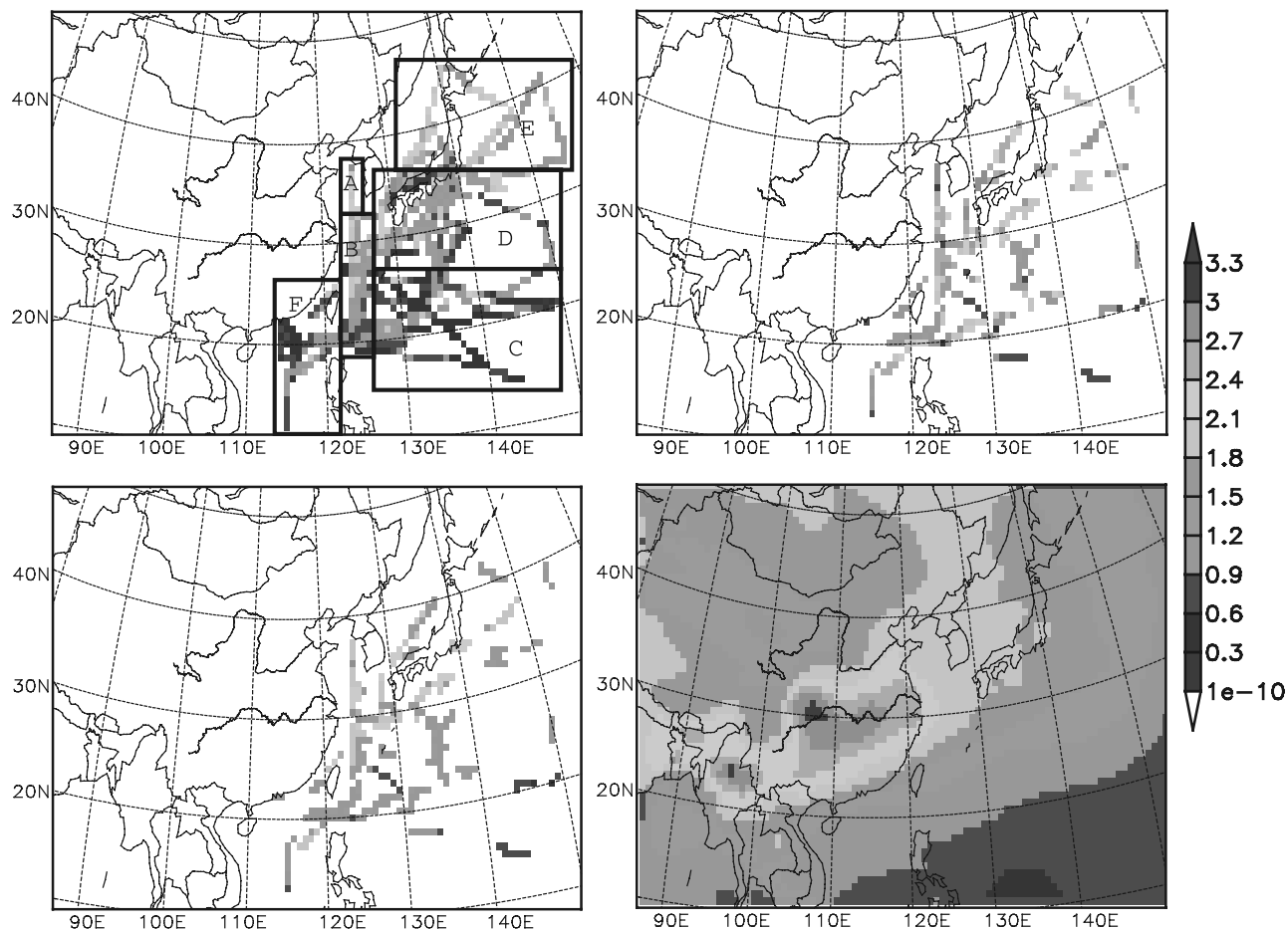
Figure 17. Mission-perspective ethane distributions (ppbv). (1) Averaged observed distribution using all P3 and DC8 5-minute merged data (upper left). (2) Averaged observed distribution using the P3 and DC8 5-min merged data for the altitude-range 0−2 km (upper right). Same as 2 but based on predicted values sampled and averaged for the same flight segments (lower left). Model calculated mean values using all modeled values between 0800 and 1800 and 0−2 km for the month of March (lower right). The zones identified are used to calculate the vertical profiles shown in Figure 18. See color version of this figure at back of this issue.

in Figure 18. These results clearly illustrate the fact that the focus on sampling frontal events resulted in a biased sampling of high concentrations. Taking SO_2 in Region-B as an example, the modeled and observed profiles when sampled together show consistent profiles, with the modeled peak value lower than the observed (as discussed previously). However, we see that the monthly mean values in the boundary layer with perfect sampling are ∼80% lower than the model values calculated using TRACE-P sampling. In the case of SO_2 the largest differences are in the lowest 2 km. For ozone the effects extend throughout the troposphere.

[48] The impact of sampling strategy on the ensemble mean distribution of select species is presented in Table 4. Shown are the percent differences ([TRACE-P]-sampling − perfect sampling)/(perfect sampling) calculated using the modeled values. Zones A−C contain only ocean points, while zones D−F contain some land points (and emission regions) as well. In the Yellow Sea (zone-A) we find that the TRACE-P sampling strategy leads to an overestimation of the mean value by 10 to 20% for CO and SO_2 at 500 m, and

10 to 30% at 3500 m. In zone-B the differences are even higher (exceeding 70% for SO_2). Impacts of sampling are largest in zone-C (e.g., 166% for SO_2). In the case of a soluble species like SO_2 this reflects in part different flow conditions, as well as the influence of wet removal (most flights attempted to avoid flying through precipitating systems). The impacts of sampling strategy on OH and HO_2 were large and could be either positive or negative. The sign reflects changes in NO_x. For example, negative changes in HO_x occur in association with positive changes in NO_x (e.g., zones B and F below 500 m).

3.6. Ozone Production in East Asia

[49] Emissions of NO_x and NMHCs have increased significantly over the last decade in Asia, and as a result urban and regional ozone levels have increased [*van Ardenne et al.*, 1999]. The TRACE-P experiment provided an opportunity to gain insight into ozone production in the region and to evaluate how well current emission estimates and models can represent the photochemical oxidant cycle in this region. As discussed previously, the model is able to
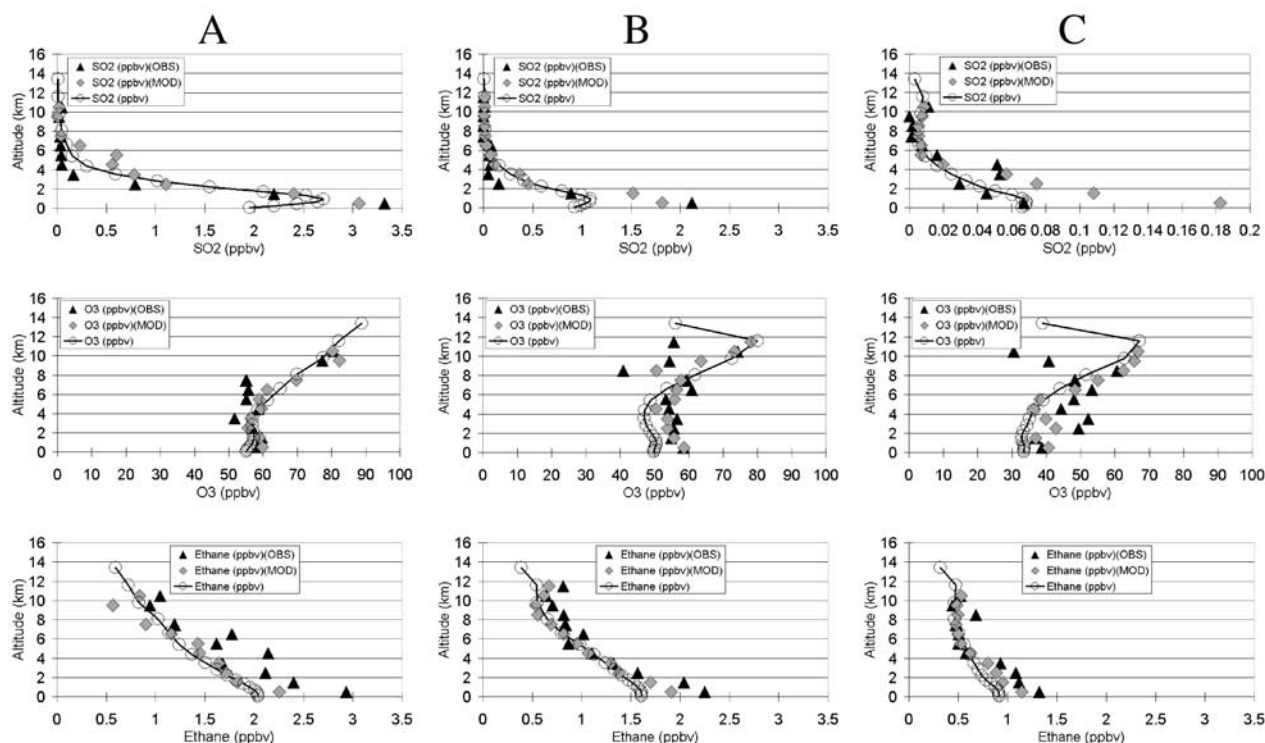
Figure 18. Calculated vertical profiles for zones A, B, and C shown in Figure 17. Shown are the vertical profile of the average value within 500m bins of the all the observations using all P-3B and DC8 5-min merged data (Obs). The calculated profiles using calculated values sampled the same way as the aircraft data are also shown (Mod). The continuous line shows the profiles calculated from perfect sampling (day-time only) within the zone.

predict with some skill the major species and parameters involved in the photochemical oxidant cycle including NO_x, NMHCs, OH, O_3, and photolysis rate, especially in the lowest few kilometers. These results provide the basis upon which to begin to explore ozone production and its sensitivity to NO_x and NMHC emissions in East Asia. A comprehensive evaluation of emission estimates is the focus of *Carmichael et al.* [2003].

[50] Insights into ozone production can be obtained using observation-based analysis. One commonly used measure of ozone production is derived from the relationship between ambient ozone and NO_z ($NO_z = NO_y - NO_x$) levels. The observed relationship from the aircraft observations is shown in Figure 19. The mission-wide data show different behavior at low and high NO_z levels. The low NO_z values correspond to high altitude data, while the high NO_z values are associated with low altitude data. We used the back-trajectory analysis discussed previously to classify the observations according to the geographical origin of the air masses and used these points to estimate an ozone production efficiency. To illustrate, the points identified as being most heavily influenced by emissions from Shanghai and

Table 4. Impact of Sampling Strategy on Mean Concentrations Expressed as Percent Difference Between Values Calculated When Sampled Using the TRACE-P Sampling Strategy and Those Calculated for the Daytime Monthly Mean (March)[a]

	Zone A		Zone B		Zone C		Zone D		Zone E		Zone F	
	500 m	3500 m	500 m	3500 m	500 m	3500 m	500 m	3500 m	500 m	3500 m	500 m	3500 m
O_3, ppbv	7	−1	17	15	21	13	6	3	10	4	18	1
NO, ppbv	26	−13	56	−2	−14	11	−43	−22	−81	−7	111	−25
NO_2, ppbv	−7	−2	14	−18	70	11	−20	15	−66	16	45	−12
OH, ppbv	25	31	−20	−1	−33	0	10	−20	−18	−34	−15	14
HO_2, ppbv	36	25	−20	3	−24	17	18	−26	140	−18	−1	−3
SO_2, ppbv	22	32	73	33	166	130	31	−20	110	39	−39	−46
SO_4, ppbv	22	44	41	15	69	51	32	−9	68	19	23	−17
CO, ppbv	15	11	6	1	13	27	9	−10	0	−4	4	−16
Ethane, ppbv	12	9	19	4	26	21	17	−2	−3	−2	8	−18
Propane, ppbv	11	10	27	3	62	49	25	−5	−9	−3	0	−39
HCHO, ppbv	4	37	16	−9	−9	−3	0	0	−21	2	13	−22

[a]The regions are shown in Figure 17 and sample vertical profiles are shown in Figure 18.
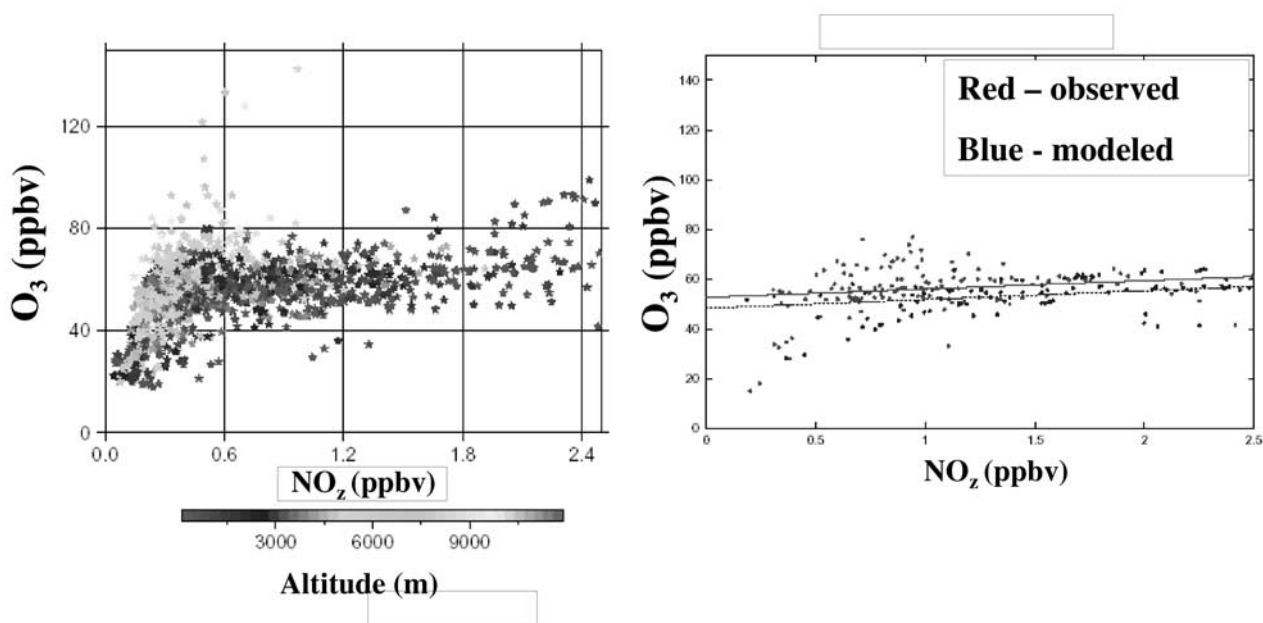
Figure 19. Observed relationship between O_3 and NO_z based on DC8 and P3 data (5-min merged) colored in altitude of the observation (a); ozone production efficiencies for points identified by back trajectory analysis to have passed over Central China at altitudes below 2 km (b). The red dots represent the observation points identified by the back-trajectory analysis; the blue dots represent the model values for these same points. See color version of this figure at back of this issue.

central China are highlighted in Figure 19, and the observed ozone production efficiency was calculated to be 3.4. The model-based analysis is also shown, and the estimated production efficiency is 3.5. The values derived from the observations for various regions are shown in Table 5. The ozone production rates vary dramatically from region to region. While these rates can only be considered qualitative (and with a high level of uncertainty), they do illustrate how information can be mined from the observations with the assistance from models.

[51] The comprehensive measurements of key photo-chemical species during TRACE-P provide valuable insights into what controls the production of ozone. Of fundamental importance to understanding what limits ozone production is a determination of whether the loss processes of HO_x are controlled by NO_x or NMHC reactions. *Kleinman* [2000] developed a procedure to estimate these processes from measured or modeled quantities. Shown in Figure 20 is the model-derived ratio of radical loss by NO_x processes (LN) to total radical production (Q) as a function of NO_x levels for all DC-8 and P-3B data points below 3 km. In this analysis, values of LN/Q above 0.5 indicate air masses in which ozone production is hydrocarbon limited and values less than 0.5 indicate conditions where ozone production is NO_x limited. Also shown are data points identified to have been influenced by emissions from megacities and the age of these air masses as determined by back trajectory analysis. We see many situations where ozone production is hydrocarbon limited, and these are not solely limited to air masses that are less than 1 day old. The majority of the

data points indicate NO_x limited conditions. Again these are not only restricted to aged air masses.

[52] We further explored the relative importance of NO_x and NMHC in ozone production in East Asia by performing model calculations for the month of March for cases where we doubled energy-related (i.e., biofuel and fossil fuel) NO_x and NMHC emissions separately. The change in ozone for each of the data points along the flight paths of the DC-8 and P-3B are presented in Figure 21. We see again that the majority of the data points indicate NO_x-limited conditions (i.e., ozone increases when NO_x emissions increase). However we see regions where O_3 decreases with increases in NO_x, as well as cases where ozone decreases with increasing NMHC, and where increasing NMHC increases ozone. Analysis of back trajectories (not shown) for the data points where ozone decreased with increasing NO_x found that all had trajectories from Tokyo, Seoul, Shanghai, and coastal areas of NE China. (In general, the negative NO_x response and positive NMHC responses are corresponding points.)

Table 5. Ozone Production Efficiencies (O_3/NO_z) Estimated From the Aircraft Observations Using Regional Classification Based on Back Trajectory Analysis

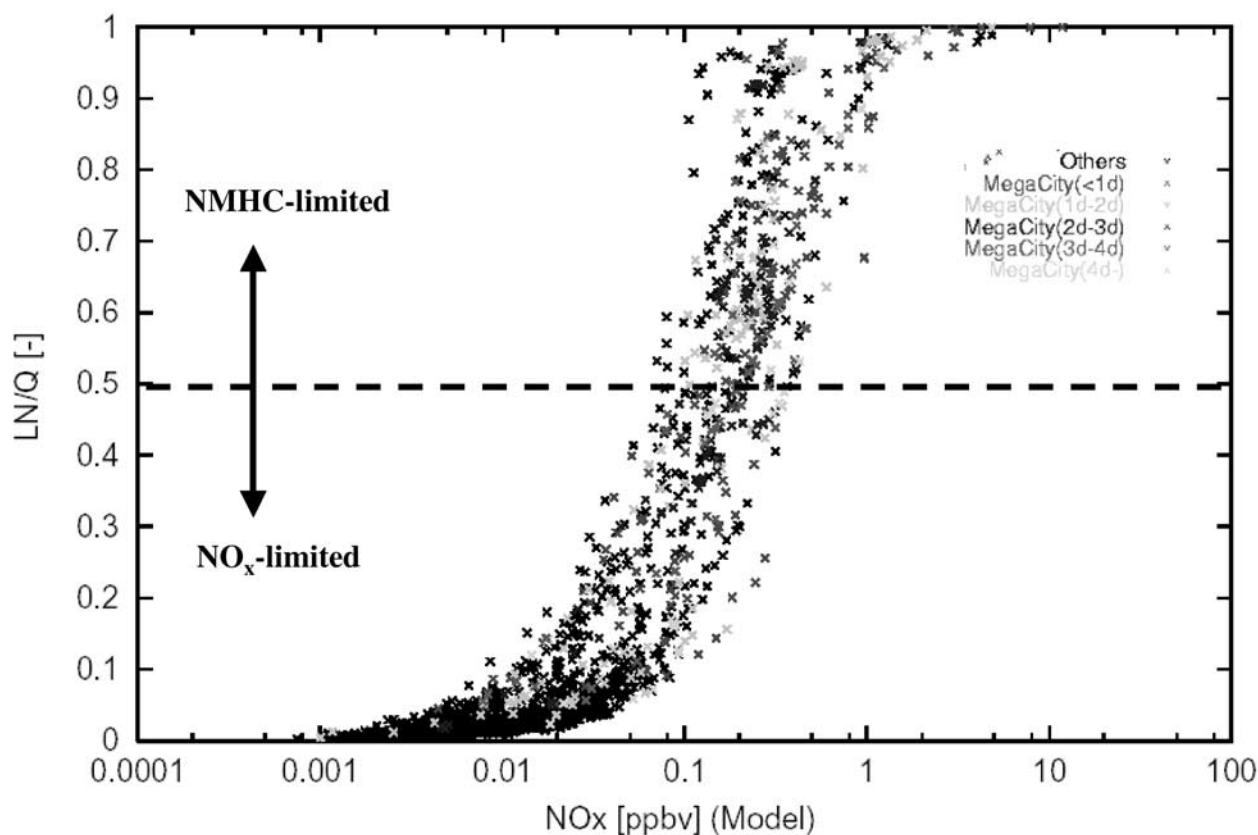| Region	O_3/NO_z
Biomass Burning (SE–Asia)	16.2
Philippine	38.1
South China	15.1
Middle China	3.4
N. China, Korea	0.8
Japan	16.3

Figure 20. Calculated ratio of radical loss due to nitrogen-oxide related processes (LN) to total radical loss (Q), for each 5-min segment of the DC8 and P3 data. Also shown is the estimated age of the air mass from passing over a major city within 2 km as determined by the back trajectory analysis. See color version of this figure at back of this issue.

This is more clearly seen in the March-averaged change in near surface ozone. The area of decreases in ozone due to increases in NO_x reflects the highly industrialized regions of East Asia, where fossil fuel usage dominates. South of $\sim 30-35N$, ozone production is NO_x-limited, reflecting the high $NMHC/NO_x$ ratios due to the large contributions to the emissions from biomass burning, biogenic sources, and biofuel usage in central China and SE Asia.

4. Summary

[53] In this paper we presented a variety of results and analysis focused on testing the capabilities of the CFORS/STEM-2K1 model to represent and help interpret the observed features of trace gas distributions in the western Pacific.

4.1. How Well Did Our Regional CTM and Estimated Emissions Represent the TRACE-P Observations?

[54] Through comparison of observed and modeled values from a mission-wide perspective, along flight paths, and by analysis of latitudinal distributions and vertical profiles, the model was shown to accurately predict many of the observed features. The model was able to represent many of the important spatial features in the observed trace species distributions, including the horizontal and latitudinal varia-

tions. Most species showed an increase in value with increase in latitude, reflecting the latitudinal distribution of emissions in East Asia. Those species with significant emissions from biomass burning (e.g., CO) showed significant enhancements also at 20–30N, which is the major outflow zone of biomass emissions from SE Asia during March.

[55] The model was shown to perform best for the lowest few kilometers of the atmosphere. In this region, the mean values calculated by the model were within ±30% of the observed values for all the parameters, and the correlation coefficients were greater than ~ 0.7 for 21 of 31 parameters and exceed 0.5 for all parameters except NO_2 and NO. It was found that the meteorological parameters were modeled most accurately, reflecting the large amount of observational data ingested into the reanalysis of the large-scale meteorological fields. The model has less skill in calculating the chemical and aerosol species. Among the trace species, ethane, propane, and ozone showed the highest values ($0.8 < R < 0.9$), followed by CO, SO_2, and NO_y. NO and NO_2 had the lowest values ($R < 0.4$). Away from the surface the performance decreased. Modeled mean values were within ±30% with the exception of RNO_3, NO_2, C_2H_6, and SO_2 in the 1–3 km region, and SO_2, NO_2, and NO for altitudes above 3 km. The vertical distributions calculated by the model captured the main features but showed less structure than observed. This was especially true above 4–5 km. This
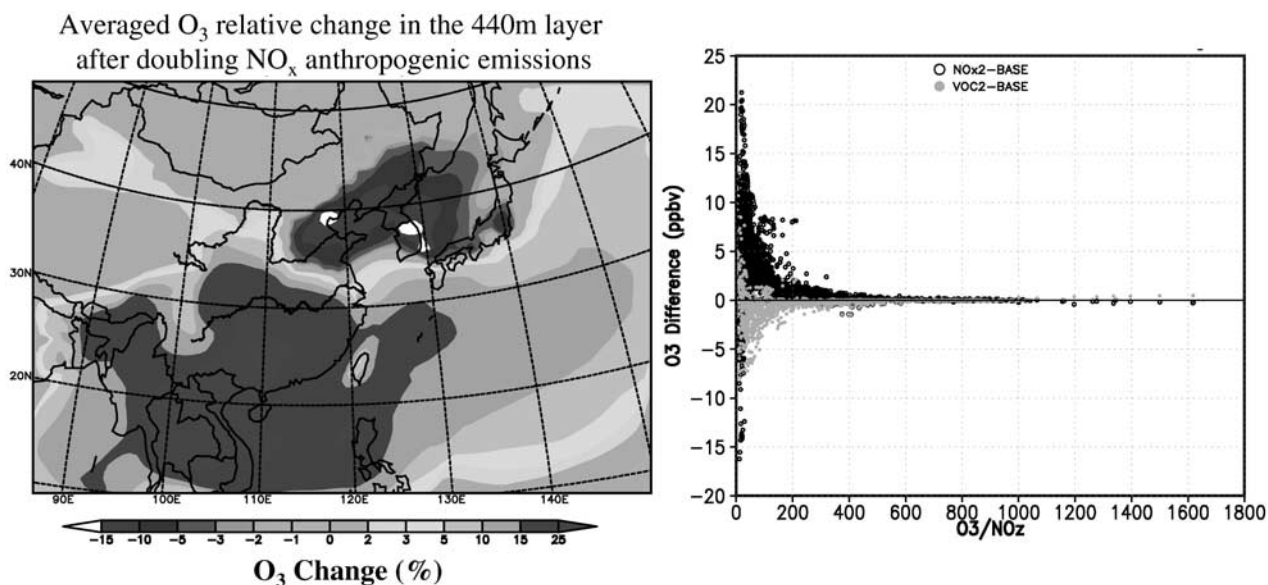
Figure 21. Average response in calculated ozone at ~500 m for the month of March due to a doubling in anthropogenic NO$_x$ emissions (left). The calculated response in ozone at the locations of the DC8 and P-3B aircraft observations for simulations where anthropogenic NO$_x$ and NMHC are increased by 2 times (separately) are also shown (right). See color version of this figure at back of this issue.

behavior reflects one of the limitations of regional models, where the upper air is dominated by the boundary conditions.

[56] The model systematically underestimated trace gas and aerosol concentrations in the marine boundary layer during flights in the Yellow Sea. Analysis showed that this was not due to displacements in the plume position (which generally were placed correctly in the model) but rather to fine scale dynamic structures that were not accurately captured in the model with 80 km horizontal resolution.

4.2. Can the Model, By Providing Temporal and Spatial Context, Aid in the Interpretation of the Aircraft Observations?

[57] Results presented demonstrate that the regional scale model that combines meteorological calculations with on-line air mass tracers, emissions, and photochemistry can provide valuable context for the interpretation of the observations. In the springtime in East Asia, cold frontal passages are the major mechanism by which pollutants are transported into the western Pacific. TRACE-P measured outflow associated with frontal events on many occasions. We used this contextual analysis to help illustrate how emissions from different parts of Asia are transported off the continent by these cold fronts. Case studies of frontal outflow and transport into the Yellow Sea were presented and showed the complex nature of outflow in East Asia. Biomass burning from SE Asia was shown to be an important source of trace species and aerosols (e.g., CO, BC, K$^+$) in the outflow and to be transported in the warm conveyor belt at altitudes above ~2 km and at latitudes below 30N. Outflow of pollution emitted along the east coast of China in the post-frontal regions was shown to be confined to the lower ~2 km and to result in high concen-

trations in the Yellow Sea. During these situations, the model under-predicted CO and BC (among other species).

[58] These results reflect the complex interactions and interdependencies between emissions, and chemical, transport, and removal processes, and the challenges we face in improving our modeling capabilities. Improvements in our ability to model trace species in East Asia will require reducing the uncertainty in emissions, better representing the dynamics in the marine boundary layer (especially under cloudy conditions) and improvements in the vertical transport processes.

[59] The impact of sampling strategy on the ensemble mean distribution of select species was also assessed. We used the model to compute the mean vertical profiles based on the observations, the model sampled the same way as the aircraft observations, and perfect sampling in the model. The results showed that the mission focus on sampling frontal events resulted in a biased sampling of high concentrations. The impact of sampling strategy on the ensemble mean distribution of species varied from 10% to 20% for CO and SO$_2$ at 500m in the Yellow Sea, to >150% for SO$_2$ the outflow regions in the western Pacific.

4.3. What Do These Results Tell Us About Our Capabilities to Characterize Ozone Production in East Asia and How Changing Trends in Emissions May Alter Ambient Ozone Levels?

[60] This question is particularly important as we try to anticipate how ozone levels in Asia will respond to changing emissions and as the region identifies and implements emission control strategies in efforts to manage local and regional ozone. One fundamental issue is whether the emission estimates are of sufficient quality to support CTM-based analysis. The TRACE-P experiment measured

a large number of parameters associated with the photochemical oxidant cycle, including precursor species, secondary products, photolysis rates, and important radicals. This data set provides an excellent opportunity to evaluate our ability to model ozone in East Asia. With this comprehensive data set we assessed with what accuracy we can model ozone in this region. We further evaluated whether the model is getting the right answers for the right reasons (i.e., is the photochemistry in the model consistent with that observed?).

[61] Based on the comparisons between observed and modeled quantities, we conclude that the emission inventory performs well for the light alkanes, ethylene, SO_2, and NO_x. Furthermore, the model showed skill in predicting important photochemical species such as O_3, PAN, HCHO, OH, HO_2, and photolysis. This implies that the emissions inventories and basic model elements are of sufficient quality to support preliminary studies of ozone production. On the other hand, the analysis pointed out problem areas as well; most notable was the tendency to underpredict CO and BC at low altitudes in the Yellow Sea. This reminding us that there still is much work to do in reducing uncertainties in Asian emissions.

[62] We have also shown how the results from this experiment could be used to assess ozone production in East Asia. Ozone is emerging as one of the primary air pollution issues in the region. However, analysis and design of control strategies is limited by the lack of detailed emissions inventories and measurements upon which to assess ozone production and to test air quality models. The TRACE-P experiment has produced a data set that we can use to test our ability to model ozone formation in East Asia (in the springtime). Form this data we have estimated ozone production efficiencies and found them to be the highest in SE Asia outflow and minimum in the Yellow Sea. We estimated the relative importance of NO_x and NMHC in ozone production in East Asia. Throughout most of the region during the period of the experiment ozone production was NO_x-limited. NMHC limited conditions were identified in the highly industrialized regions of East Asia, where fossil fuel usage dominates. South of $\sim 30-35N$, ozone production was found to be NO_x-limited, reflecting the high NMHC/NO_x ratios due to the large contributions to the emissions from biomass burning, biogenic sources, and biofuel usage in central China and SE Asia.

References

Carter, W., Documentation of the SAPRC-99 chemical mechanism for voc reactivity assessment, Final Rep. to Calif. Air Res. Board, *Contract 92-329*, Univ. of Calif., Riverside, Calif., 2000.

Collins, W., P. Rasch, B. Eaton, B. Khattatov, J. Lamarque, and C. Zender, Simulating aerosols using a chemical transport model with assimilation of satellite aerosol retrievals: Methodology for INDOEX, *J. Geophys. Res.*, *106*, 7313–7336, 2001.

Eisele, F. L., et al., Summary of measurement intercomparisons during TRACE-P, *J. Geophys. Res.*, *108*(D20), 8791, doi:10.1029/2002JD003167, in press, 2003.

Gong, S. L., L. A. Barrie, and J.-P. Blacnchet, Modeling sea-salt aerosols in the atmosphere: 1. Model development, *J. Geophys. Res.*, *102*, 3805–3818, 1997.

Guenther, A., et al., A global model of natural volatile organic compound emissions, *J. Geophys. Res.*, *100*, 8873–8892, 1995.

Huebert, B., T. Bates, P. Russell, G. Shi, Y. Kim, K. Kawamura, G. Carmichael, and T. Nakajima, An overview of ACE-Asia: Strategies for quantifying the relationships between Asian aerosols and their climatic impacts, *J. Geophys. Res.*, *108*, doi:10.1029/2003JD003550, in press, 2003.

Jacob, D., J. Crawford, M. Kleb, V. Conners, R. Bendura, J. Raper, G. Sachse, J. Gille, and L. Emmons, The transport and chemical evolution over the Pacific (TRACE-P) mission: Design, execution, and overview of first results, *J. Geophys. Res.*, *108*(D20), 8781, doi:10.1029/2002JD003276, in press, 2003.

Kiley, C., et al., Intercomparison and evaluation of aircraft-derived and simulated CO from seven chemical transport models during the TRACE-P experiment, *J. Geophys. Res.*, *108*(D21), 8819, doi:10.1029/2002JD003089, in press, 2003.

Kleinman, L., Ozone process insights from field experiments, part II: Observation-based analysis for ozone production, *Atmos. Environ.*, *34*, 2023–2033, 2000.

Lawrence, M., et al., Global chemical weather forecasts for field campaign planning: Predictions and observations of large-scale features during MINOS, CONTRACE, and INDOEX, *Atmos. Chem. Phys. Discussions*, *2*, 1545–1597, 2002.

Lee, A., G. Carver, M. Chipperfield, and J. Pyle, Three-dimensional chemical forecasting: A methodology, *J. Geophys. Res.*, *102*, 3905–3919, 1997.

Madronich, S., and S. Flocke, The role of solar radiation in atmospheric chemistry, in *Handbook of Environmental Chemistry*, edited by P. Boule, pp. 1–26, Springer-Verlag, New York, 1999.

Pickering, K. E., Y. Wang, W.-K. Tao, C. Price, and J.-F. Muller, Vertical distributions of lightning NO_x for use in regional and global transport models, *J. Geophys. Res.*, *103*, 31,203–31,216, 1998.

Pielke, R. A., et al., A comprehensive meteorological modeling system - RAMS, *Meteorol. Atmos. Phys.*, *49*, 69–91, 1992.

Rasch, P., W. Collins, and B. Eaton, Understanding the Indian Ocean Experiment (INDOEX) aerosol distributions with an aerosol assimilation, *J. Geophys. Res.*, *106*, 7337–7355, 2001.

Song, C. H., and G. R. Carmichael, A three-dimensional modeling investigation of the evolution processes of dust and Sea Salt particles in east Asia, *J. Geophys. Res.*, *106*, 18,131–18,153, 2001.

Streets, D. G., et al., An inventory of gaseous and primary aerosol emissions in Asia in the year 2000, *J. Geophys. Res.*, *108*(D21), 8809, doi:10.1029/2002JD003093, in press, 2003a.

Streets, D., K. F. Yarber, J.-H. Woo, and G. R. Carmichael, Biomass burning in Asia: Annual and seasonal estimates and atmospheric emissions, *Global Biogeochem. Cycles*, *17*, doi:10.1029/2003GB002040, in press, 2003b.

Tang, Y., et al., Impacts of aerosols and clouds on photolysis frequencies and photochemistry during TRACE-P, part II: Three-dimensional study using a regional chemical transport model, *J. Geophys. Res.*, *108*(D21), 8822, doi:10.1029/2002JD003100, in press, 2003a.

Tang, Y., et al., Influences of biomass burning during TRACE-P experiment identified by the regional chemical transport model, *J. Geophys. Res.*, *108*(D21), 8824, doi:10.1029/2002JD003110, in press, 2003b.

Tu, F., D. Thornton, A. Bandy, M.-S. Kim, G. Carmichael, Y. Tang, L. Thornhill, and G. Sachse, Dynamics and transport of sulfur dioxide over the Yellow Sea during TRACE-P, *J. Geophys. Res.*, *108*(D20), 8790, doi:10.1029/2002JD003227, in press, 2003.

Underwood, G. M., C. H. Song, M. Phadnis, G. R. Carmichael, and V. H. Grassian, Heterogeneous reactions of NO_2 and HNO_3 on oxides and mineral dust: A combined laboratory and modeling study, *J. Geophys. Res.*, *106*, 18,055–18,066, 2001.

Uno, I., et al., Regional chemical weather forecasting system CFORS: Model descriptions and analysis of surface observation at Japanese island stations during the ACE-Asia experiment, *J. Geophys. Res.*, *108*(D23), 8668, doi:10.1029/2002JD002845, 2003.

van Ardenne, J. A., G. R. Carmichael, H. Levy, D. Streets, and L. Hordijk, Anthropogenic NO_x emissions in Asia in the period 1990–2020, *Atmos. Environ.*, *33*, 633–646, 1999.

Verwer, J. G., E. J. Spee, J. G. Blom, and W. H. Hundsdorfer, A second order Rosenbrock method applied to photochemical dispersion problems, *SIAM J. Sci. Comput.*, *20*, 1456–1480, 1999.

Woo, J.-H., et al., The contribution of biomass and biofuel emissions to trace gas distributions in Asia during the TRACE-P experiment, *J. Geophys. Res.*, *108*(D21), 8812, doi:10.1029/2003JD003200, in press, 2003.

Yoshino, A., H. Nagai, N. Umeyama, and M. Chino, Real-time simulation and analysis on long range atmospheric dispersion of volcanic gases

discharged from the Miyajima Island, *J. Jpn. Soc. Atmos. Environ.*, *37*, 23–34, 2002.

Zhang, M., et al., Large-scale structure of trace gas and aerosol distributions over the western Pacific during TRACE-P, *J. Geophys. Res.*, *108*(D21), 8820, doi:10.1029/2002JD002946, in press, 2003.

———————————

E. Apel, E. Atlas, C. Cantrell, F. Eisele, A. Fried, B. Lefer, and R. Shetter, National Center for Atmospheric Research, Boulder, CO 80305, USA. (apel@ucar.edu; atlas@ucar.edu; lcantrell@ucar.edu; eisele@ucar.edu; fried@ucar.edu; lefer@ucar.edu; shetter@ucar.edu)

M. Avery and J. Barrick, Atmospheric Sciences Competency, NASA Langley Research Center, Hampton, VA 23681, USA. (m.a.avery@larc.nasa.gov; j.d.barrick@larc.nasa.gov)

A. Bandy, G. Sachse, and D. Thorton, Chemistry Department, Drexel University, Philadelphia, PA 19104, USA. (bandyar@drexel.edu; dct@drexel.edu)

D. Blake, Department of Chemistry, University of California, Irvine, Irvine, CA 92697, USA. (drblake@uci.edu)

W. Brune, Department of Meteorology, Pennsylvania State University, University Park, PA 16802, USA. (brune@essc.psu.edu)

G. R. Carmichael, H. Huang, Y. Tang, J.-H. Woo, and J. Yienger, Center for Global and Regional Environmental Research, University of Iowa, Iowa City, IA 52242, USA. (gcarmich@engineering.uiowa.edu; huang@cgrer.uiowa.edu; ytang@cgrer.uiowa.edu; woojh21@cgrer.uiowa.edu; jyienger@cgrer.uiowa.edu)

A. Clarke, School of Ocean and Earth Science and Technology, University of Hawaii at Manoa, Honolulu, HI 96822, USA. (tclarke@soest.hawaii.edu)

B. Heikes, Graduate School of Oceanography, University of Rhode Island, Narragansett, RI 02882, USA. (bheikes@gso.uri.edu)

Y. Kondo, Research Center for Advanced Science and Technology, University of Tokyo, Meguro-ku, Tokyo 153-8904, Japan. (kondo@atmos.rcast.u-tokyo.ac.jp)

G. Kurata, Department of Ecological Engineering, Toyohashi University of Technology, Toyohashi, Aichi 441-8580, Japan. (kurata@eco.tut.ac.jp)

S. Sandholm, School of Earth and Atmospheric Sciences, Georgia Institute of Technology, Atlanta, GA 30332, USA. (scott.sandholm@eas.gatech.edu)

H. Singh, NASA Ames Research Center, Moffett Field, CA 94035, USA. (hanwat.b.singh@nasa.gov)

D. Streets, Decision and Information Sciences Division, Argonne National Laboratory, Argonne, IL 60439, USA. (dstreets@anl.gov)

R. Talbot, Institute for the Study of Earth, Oceans, and Space, University of New Hampshire, Durham, NH 03824, USA. (robert.talbot@unh.edu)

I. Uno, Research Institute for Applied Mechanics, Kyushu University, Fukuoka 816-8580, Japan. (iuno@riam.kyushu-u.ac.jp)
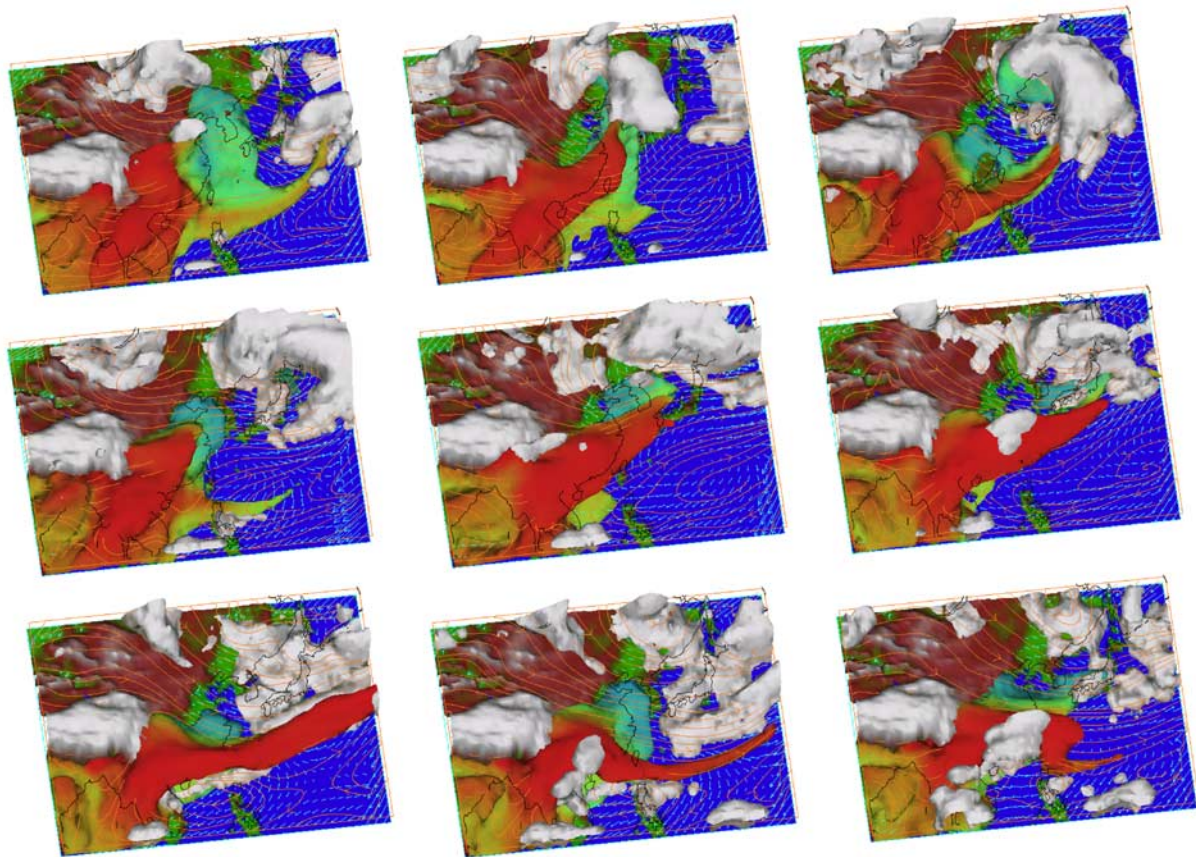
Figure 2. Forecasts of pollution outflow during the frontal events of 2 March (top left) through 10 March (lower right). Shown are clouds (white), BC isosurface (>1μg/m3) colored by percent due to biomass burning (red > 50%), 3 km streamlines (orange), wind vectors at 600 m (blue) at 6 GMT. The green-brown-gray shading represents the topography in the region (from low to high). The Tibet Plateau is white in these images.
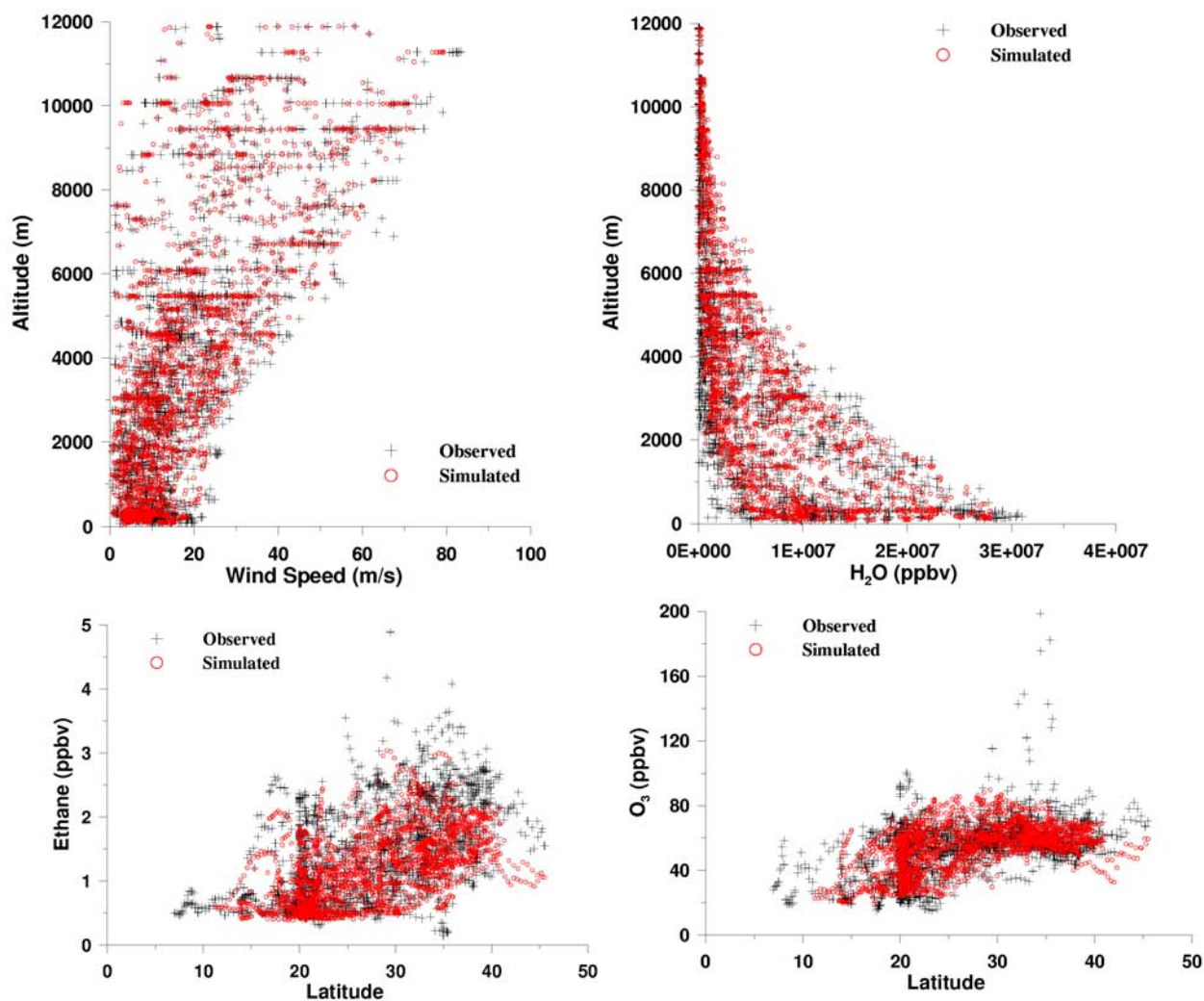
Figure 3. Measured and modeled vertical distributions of wind speed and water vapor mixing ratios (top) and latitudinal distributions of ethane and ozone (bottom) for the DC8 and P-3B aircraft data. Shown are values for each 5-min flight segments from the merged data set.
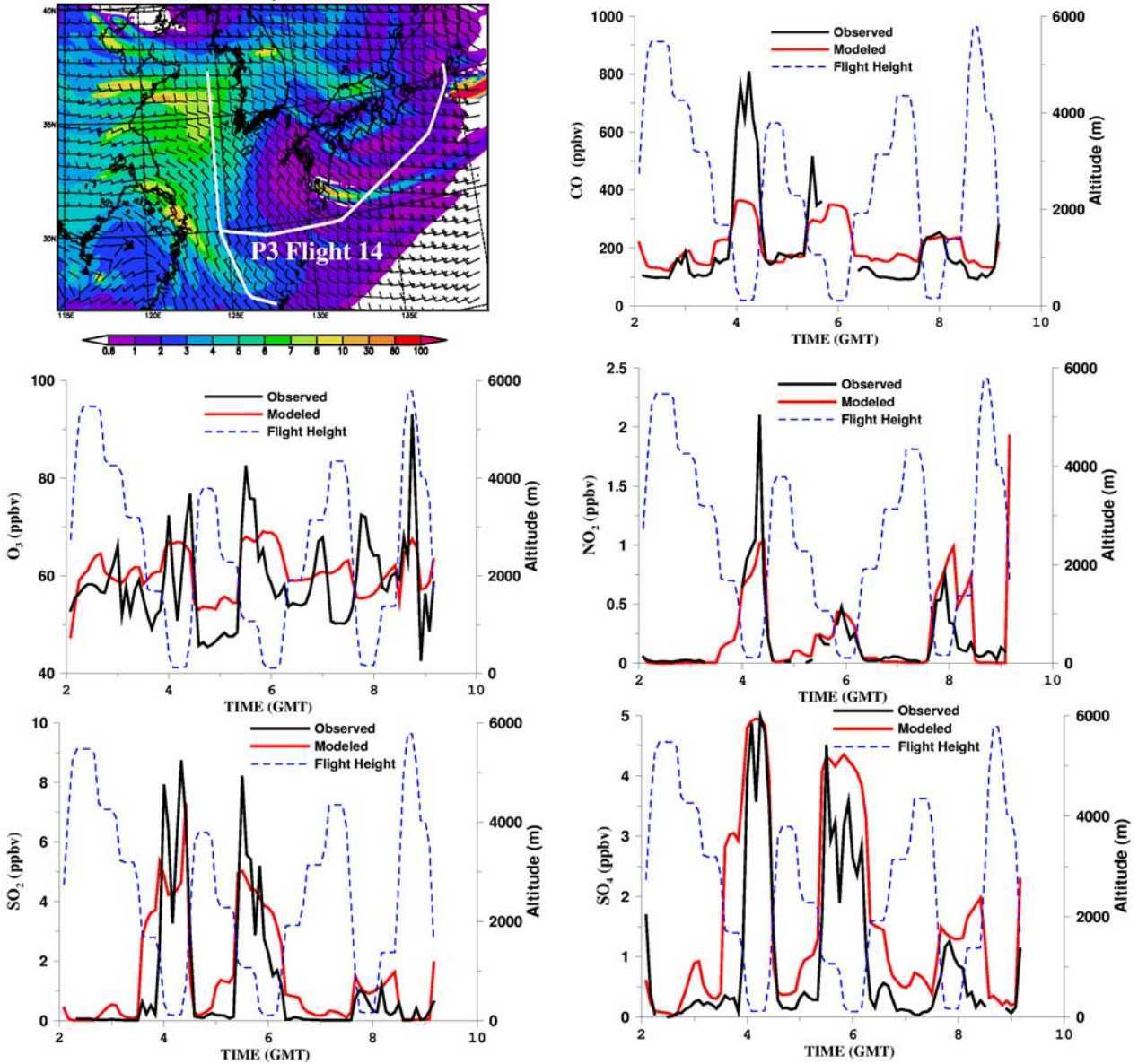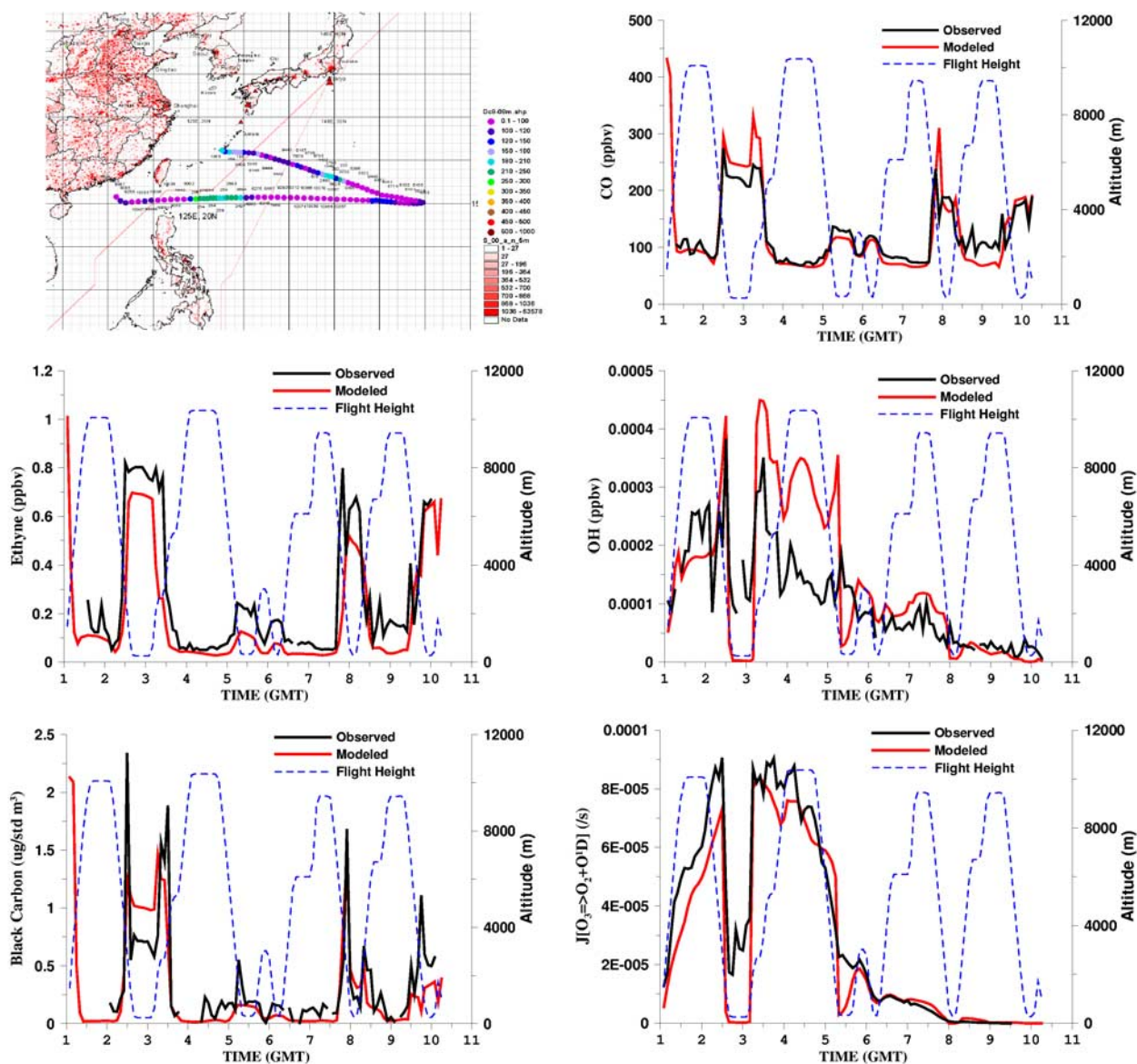
Figure 6. Comparison of observed and predicted species along the P-3B flight path on 18 March using the 5-min merged data set.

**Figure 7.** Comparison of the observed (red) and modeled (blue) vertical profiles of OH, C_2H_6, CO, and O_3 for the DC8 data. The horizontal bars indicate the $\pm$ one standard deviation for each 1 km altitude bin.
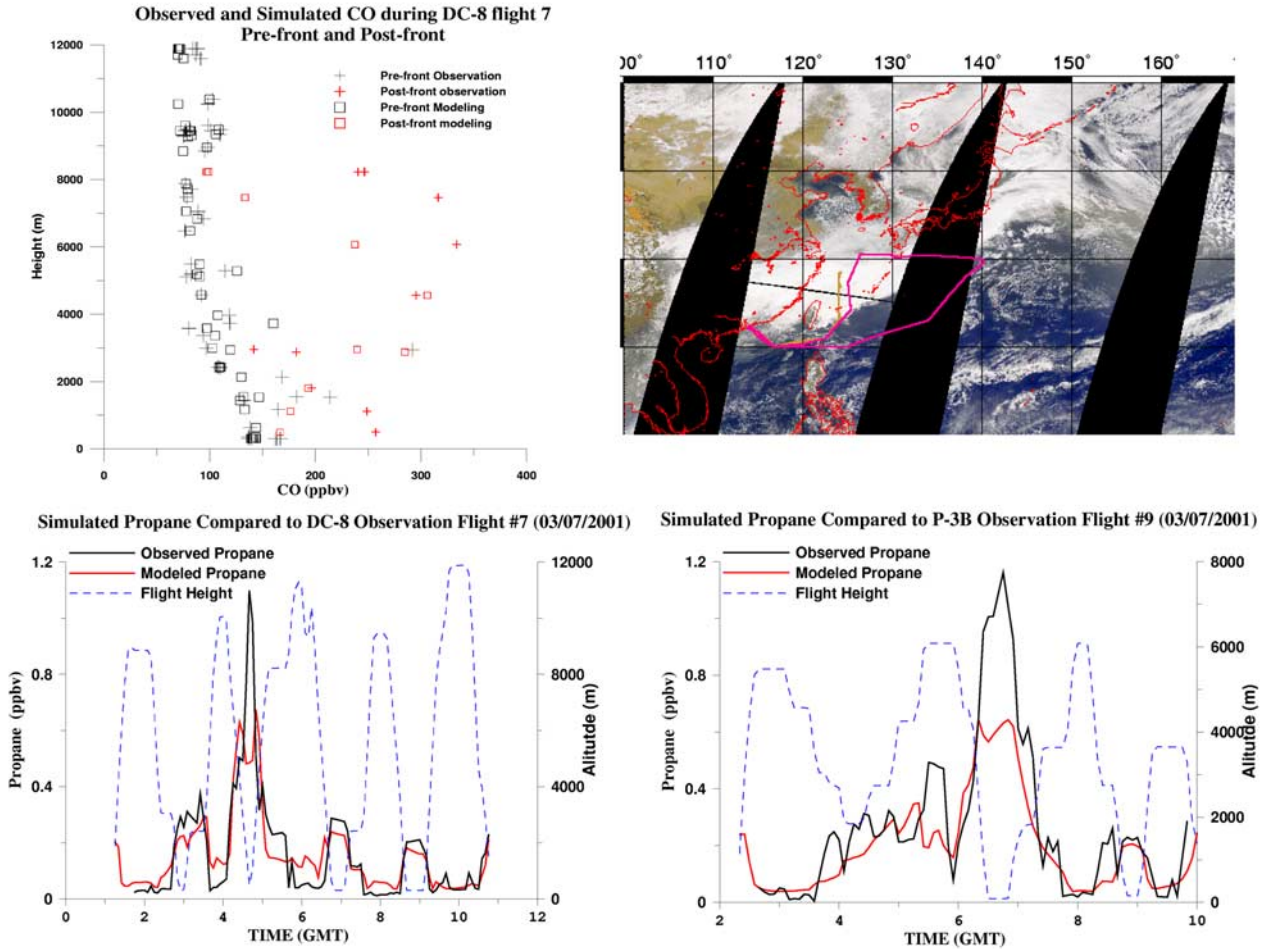
Figure 8. Observed and simulated vertical profiles of CO on DC8 flight 7 in the prefrontal and postfrontal regions. Also shown are the observed and calculated propane mixing ratios for the DC8 flight 7 and P-3B flight 9. The flight paths are also show (red is DC8; gold is P-3B).
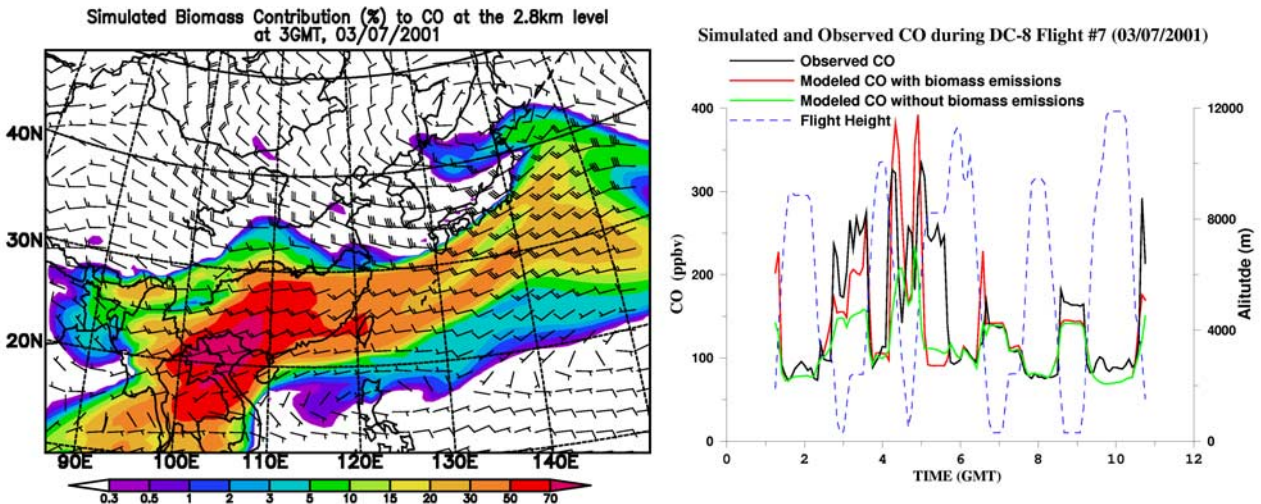
Figure 9. Observed and calculated CO for DC8 flight 7. Shown are results with and without biomass burning emissions. The contribution of CO (expressed as fraction) due to biomass burning obtained by runs with and without the biomass burning sources at 2.8 km is also shown. The flight path is shown in Figure 8.

Figure 10. Forecast of CO due to biomass burning along 20N at 3 GMT (12 Japan Standard Time (JST)) on 9 March (top). Shown is the vertical distribution of primary CO due to biomass burning. The observed total CO and aerosol potassium measured by G. Sacshe and R. Weber, respectively, are also shown. Potassium provides a good tracer for biomass burning.
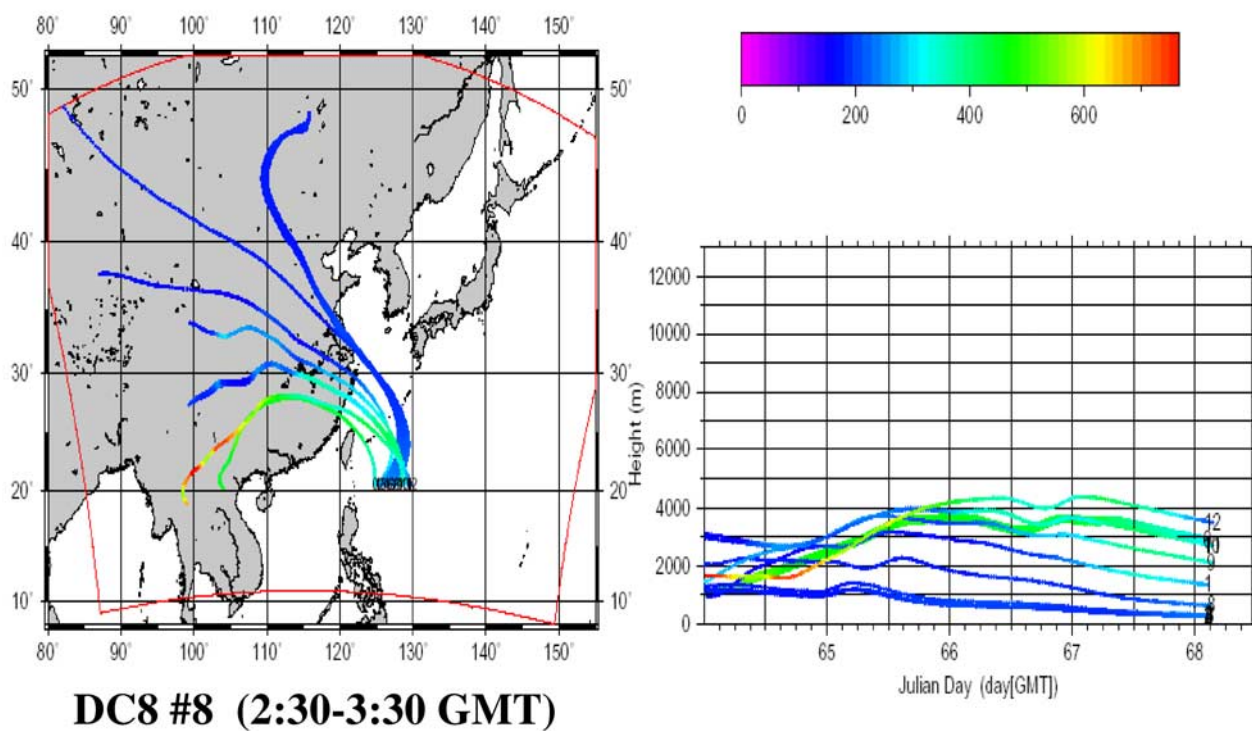
DC8 #8 (2:30-3:30 GMT)

Figure 11. Five-day back trajectories every five minutes along the DC8 flight path from 2:30–3:30 GMT for flight 8. Trajectories are colored by modeled CO.

Figure 12. Comparison of observed and predicted species along the DC8 flight 7 path on 9 March using the 5-min merged data set.
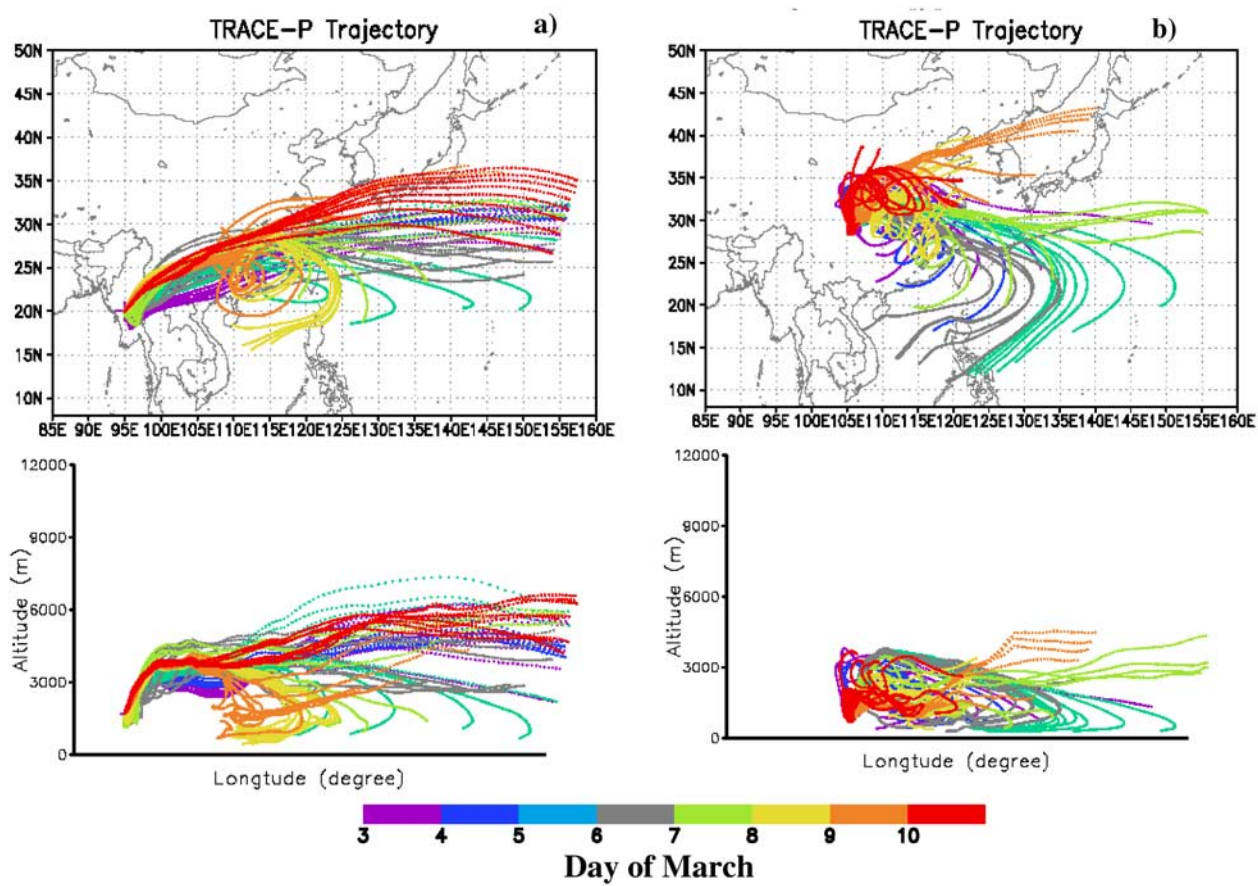
Figure 13. Five-day forward trajectories from a biomass source region in SE Asia (a), Chongqing (b), Shanghai (c), and Qingdao (d).
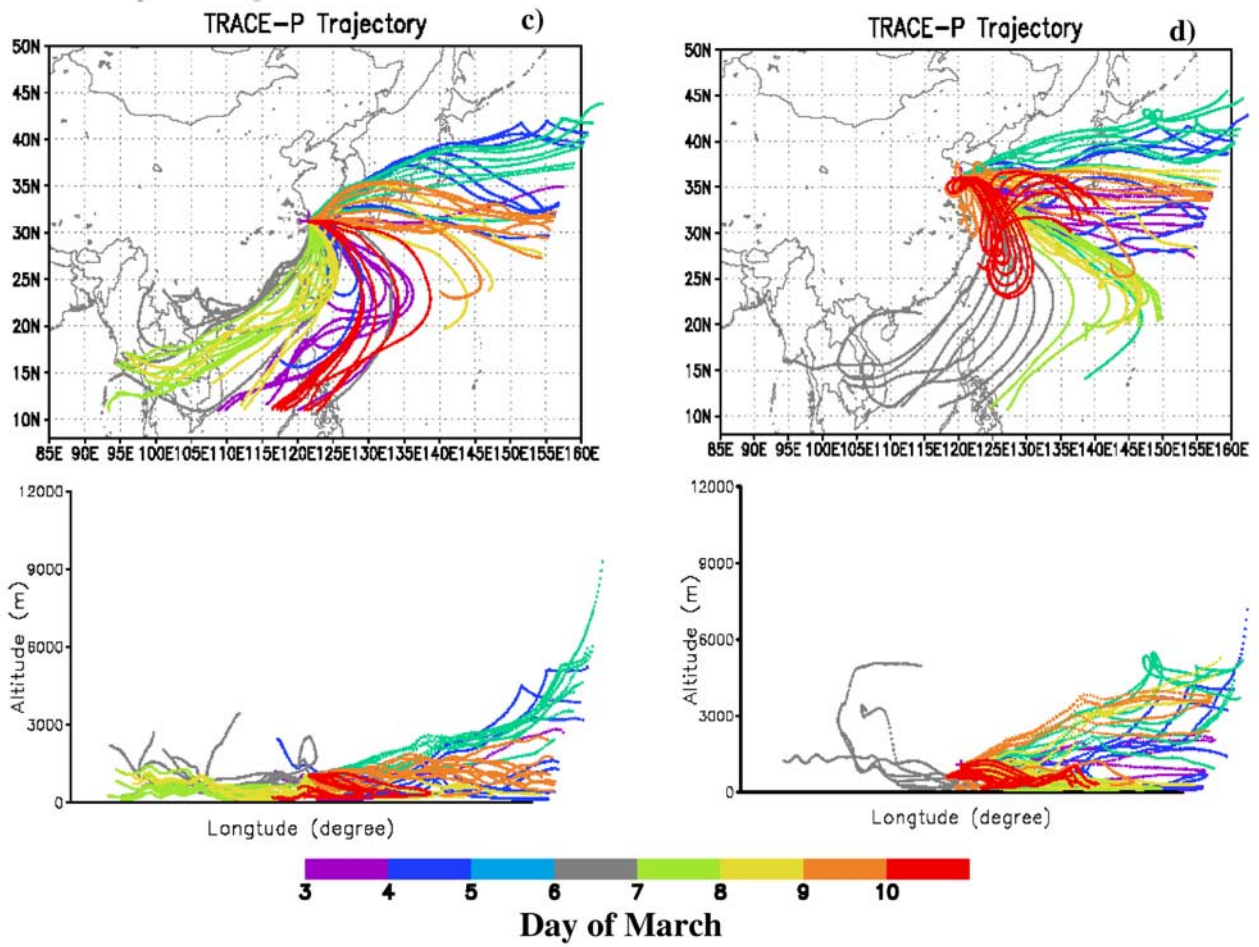
Figure 13. (continued)
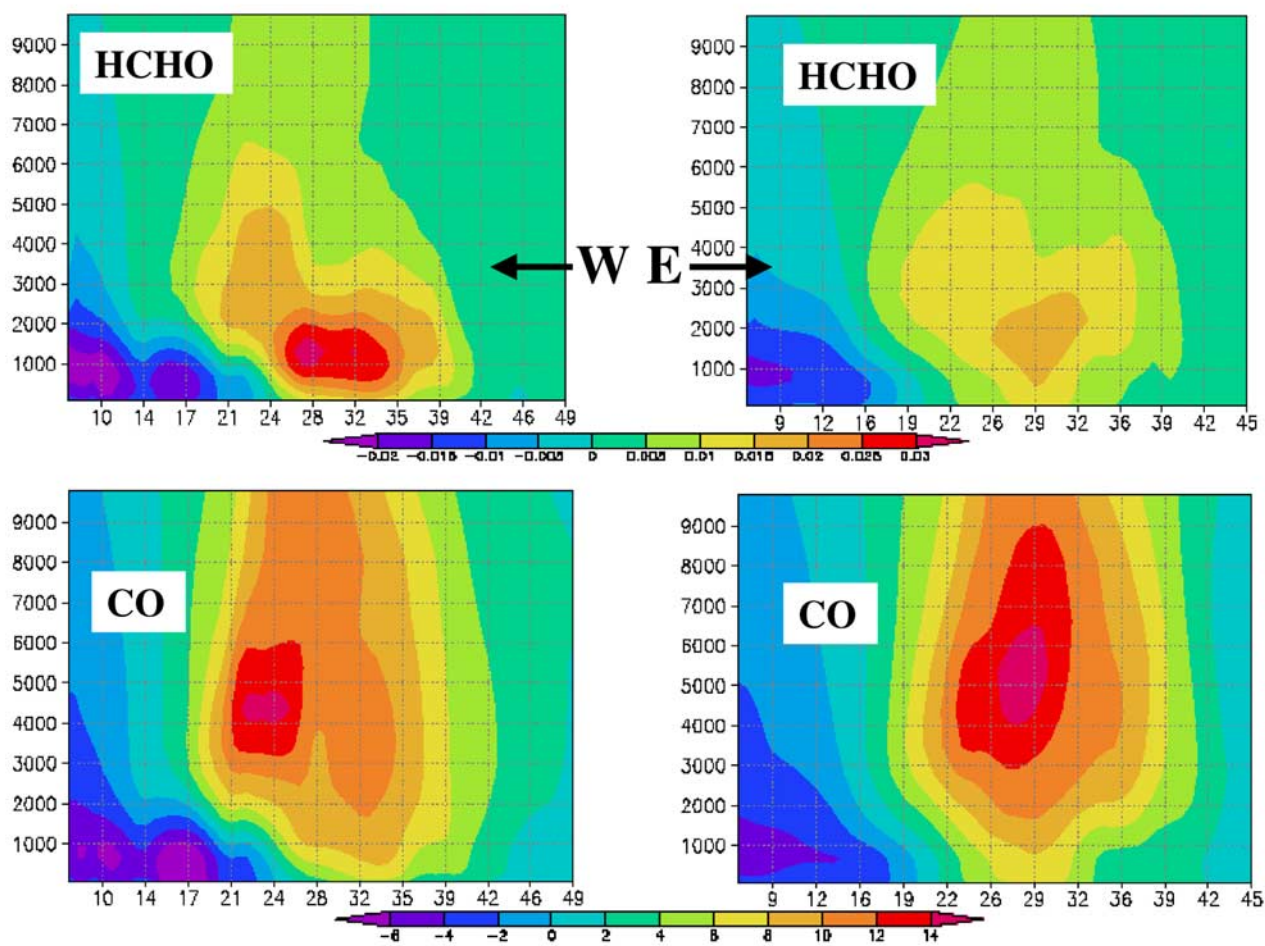
Figure 14. Calculated vertical profiles of horizontal fluxes for HCHO and CO (unit mmol/m^2/s) along the surfaces indicated averaged over 1–14 March. The west boundary is approximately 125E, the east boundary is ~145E.
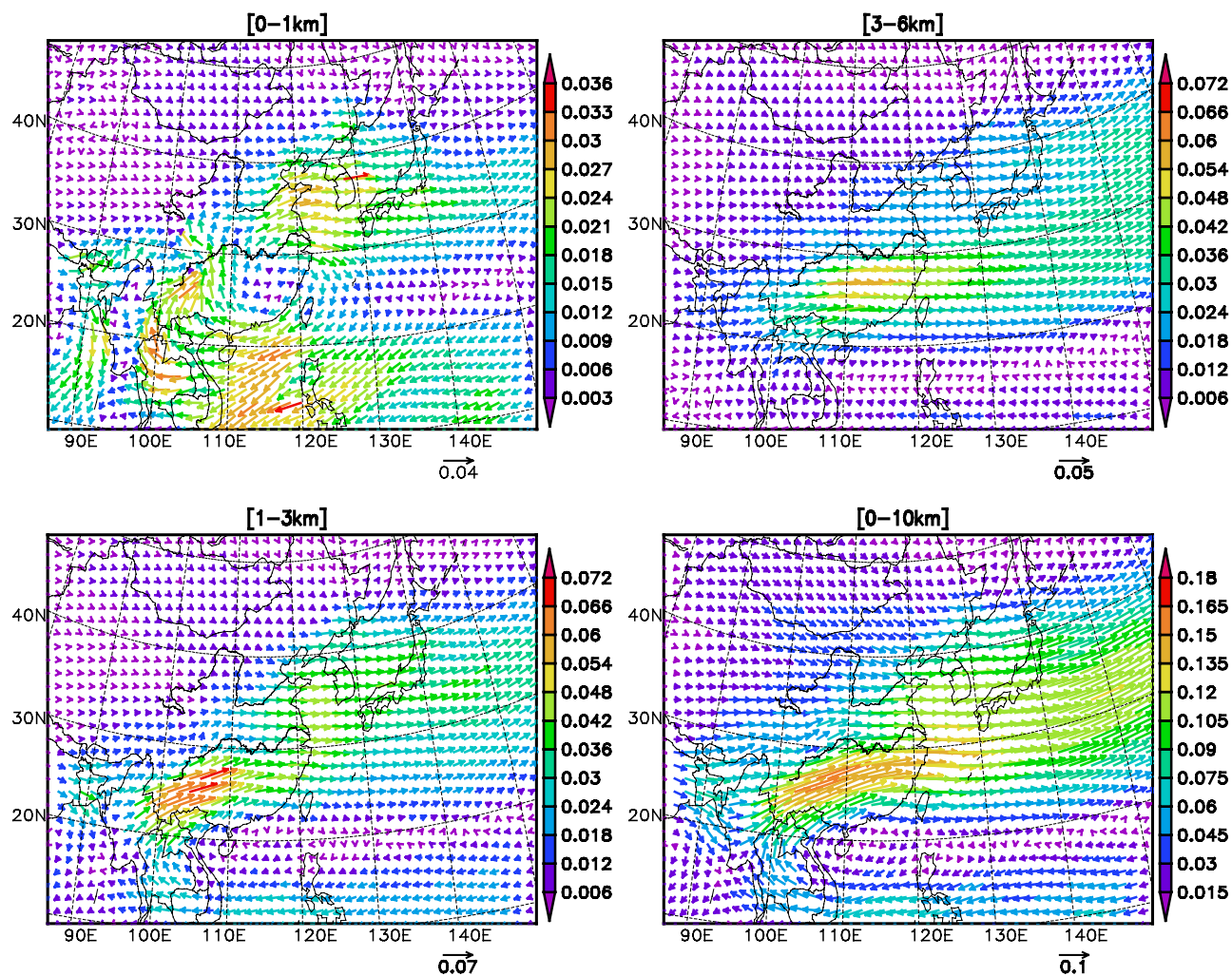
Figure 15. Calculated horizontal fluxes of HCHO (unit mol/m/s) that is vertically integrated for different vertical layers, averaged over 1–14 March. Vector indicates the flux direction. Both color and length of vector represent magnitude.
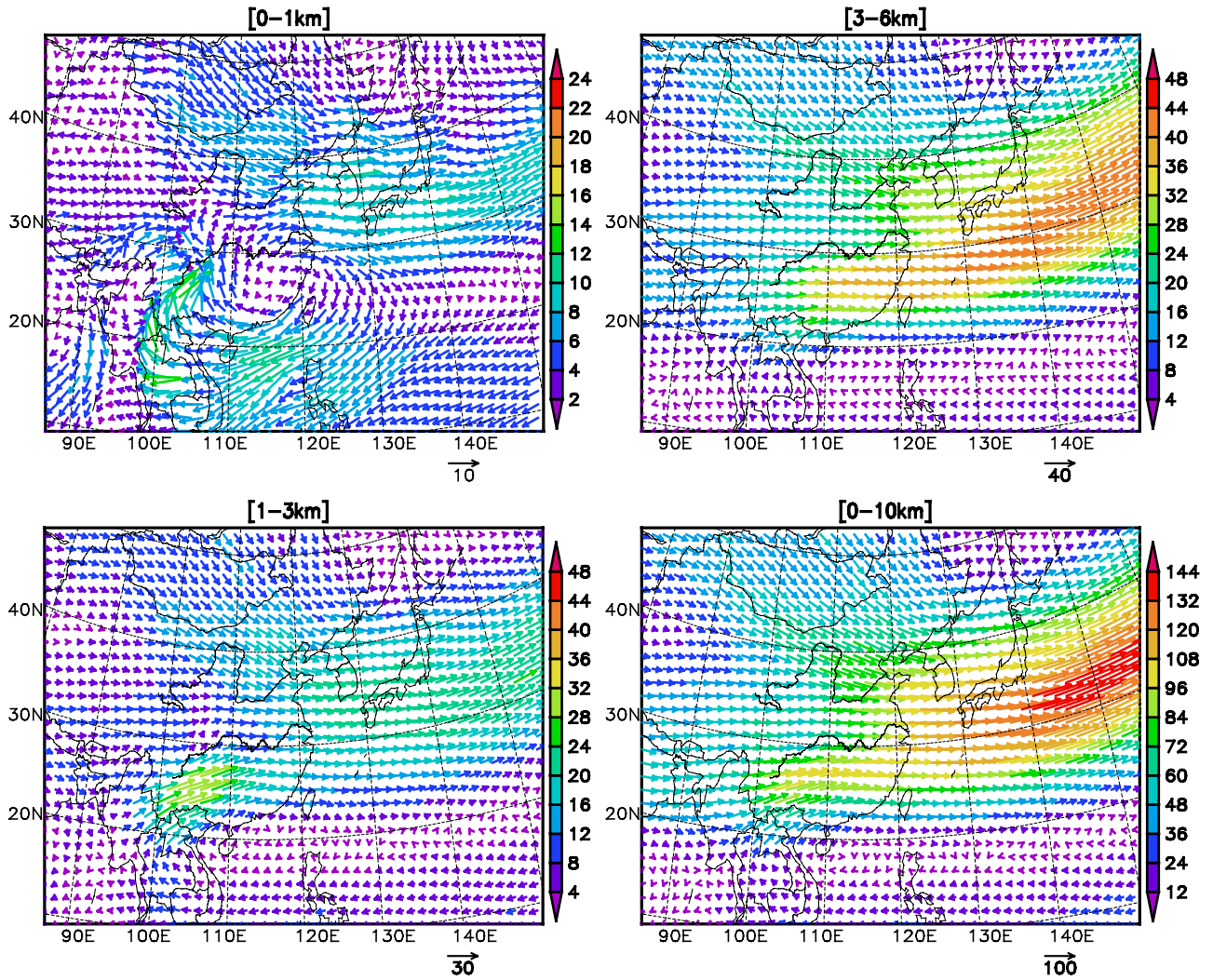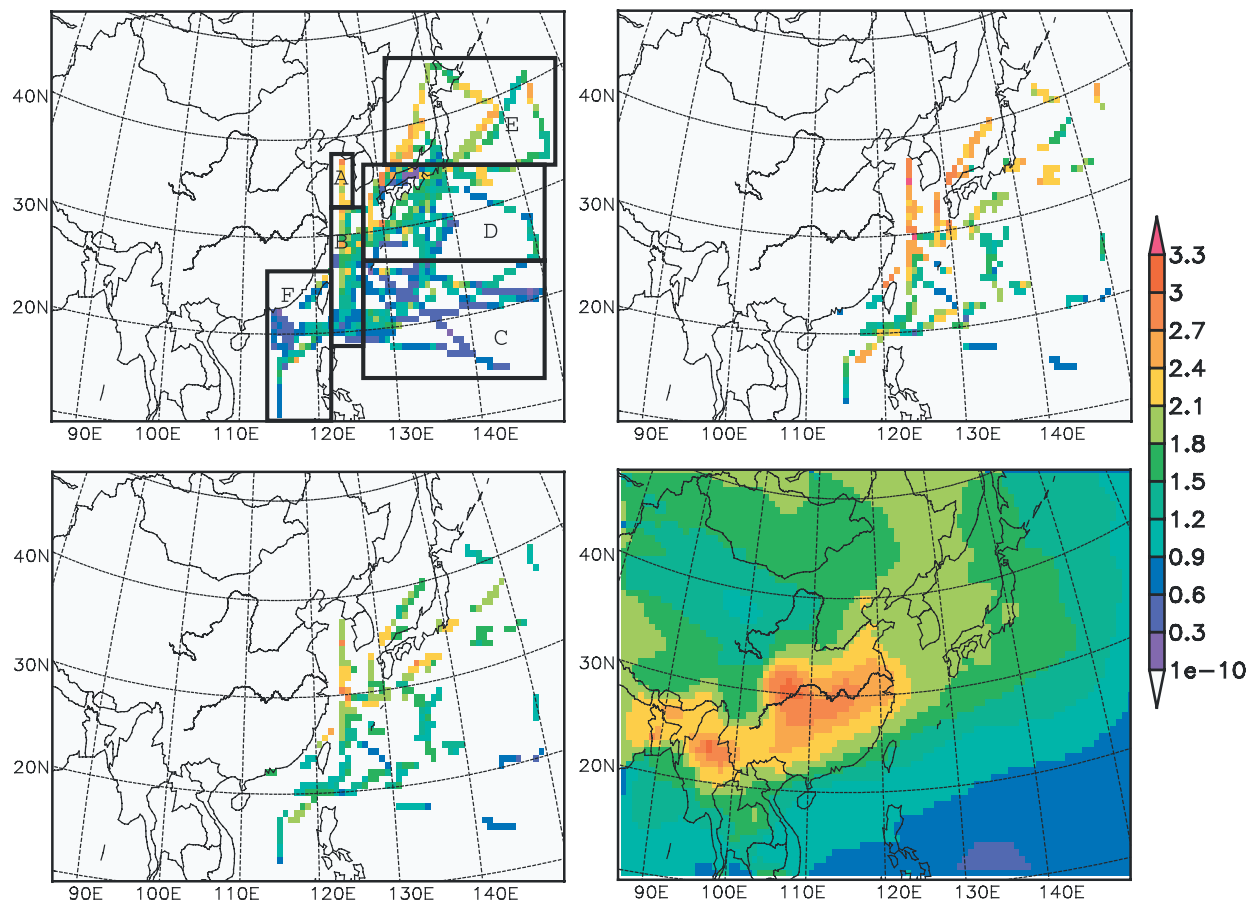
Figure 16. Calculated horizontal fluxes of CO (unit mol/m/s) that is vertically integrated for different vertical layers, averaged over 1–14 March. Vector indicates the flux direction. Both color and length of vector represent magnitude.

Figure 17. Mission-perspective ethane distributions (ppbv). (1) Averaged observed distribution using all P3 and DC8 5-minute merged data (upper left). (2) Averaged observed distribution using the P3 and DC8 5-min merged data for the altitude-range 0–2 km (upper right). Same as 2 but based on predicted values sampled and averaged for the same flight segments (lower left). Model calculated mean values using all modeled values between 0800 and 1800 and 0–2 km for the month of March (lower right). The zones identified are used to calculate the vertical profiles shown in Figure 18.
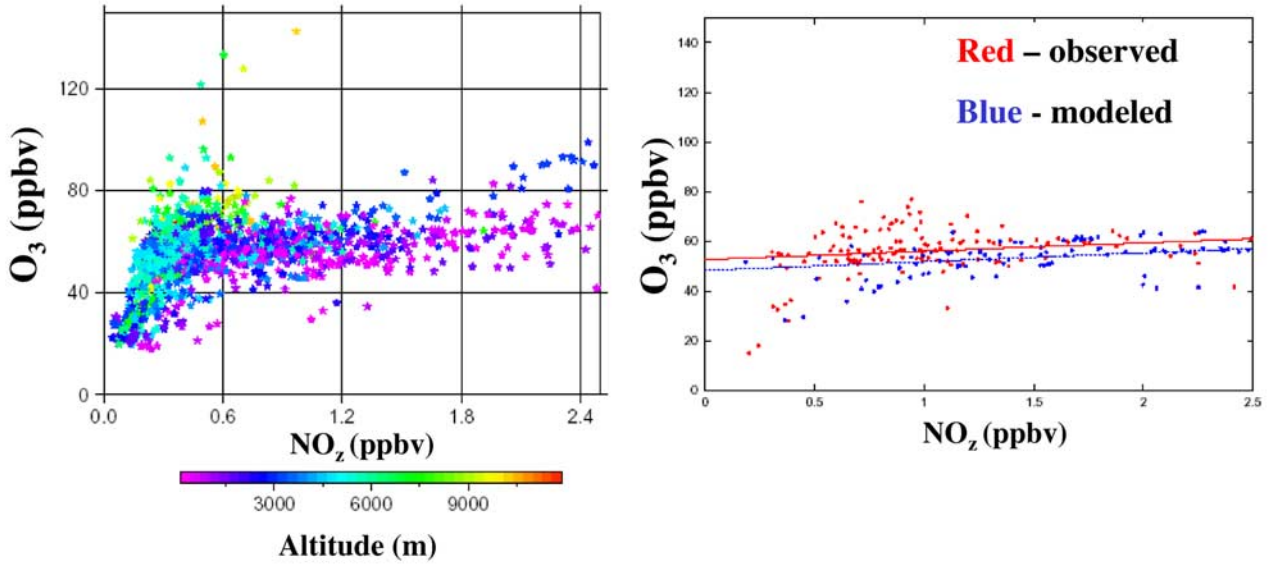
Figure 19. Observed relationship between O_3 and NO_z based on DC8 and P3 data (5-min merged) colored in altitude of the observation (a); ozone production efficiencies for points identified by back trajectory analysis to have passed over Central China at altitudes below 2 km (b). The red dots represent the observation points identified by the back-trajectory analysis; the blue dots represent the model values for these same points.
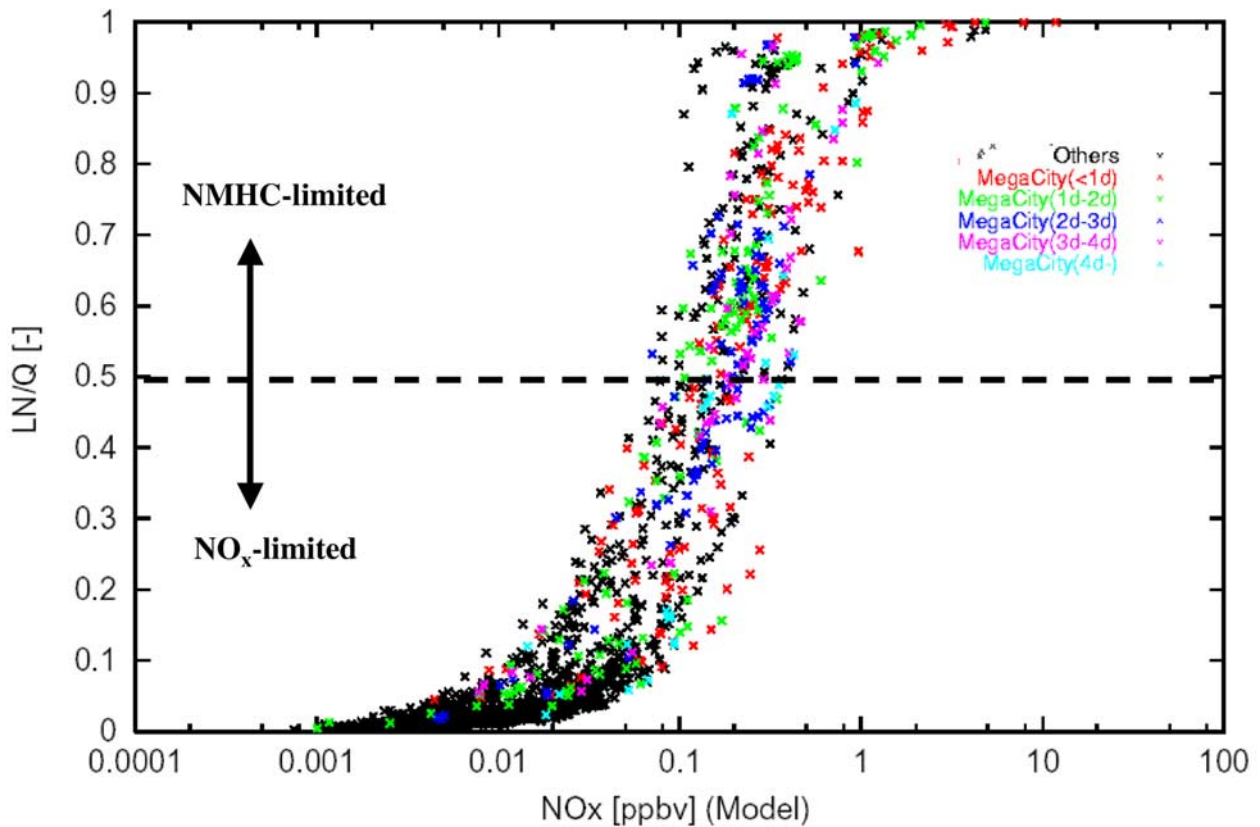

Figure 20. Calculated ratio of radical loss due to nitrogen-oxide related processes (LN) to total radical loss (Q), for each 5-min segment of the DC8 and P3 data. Also shown is the estimated age of the air mass from passing over a major city within 2 km as determined by the back trajectory analysis.
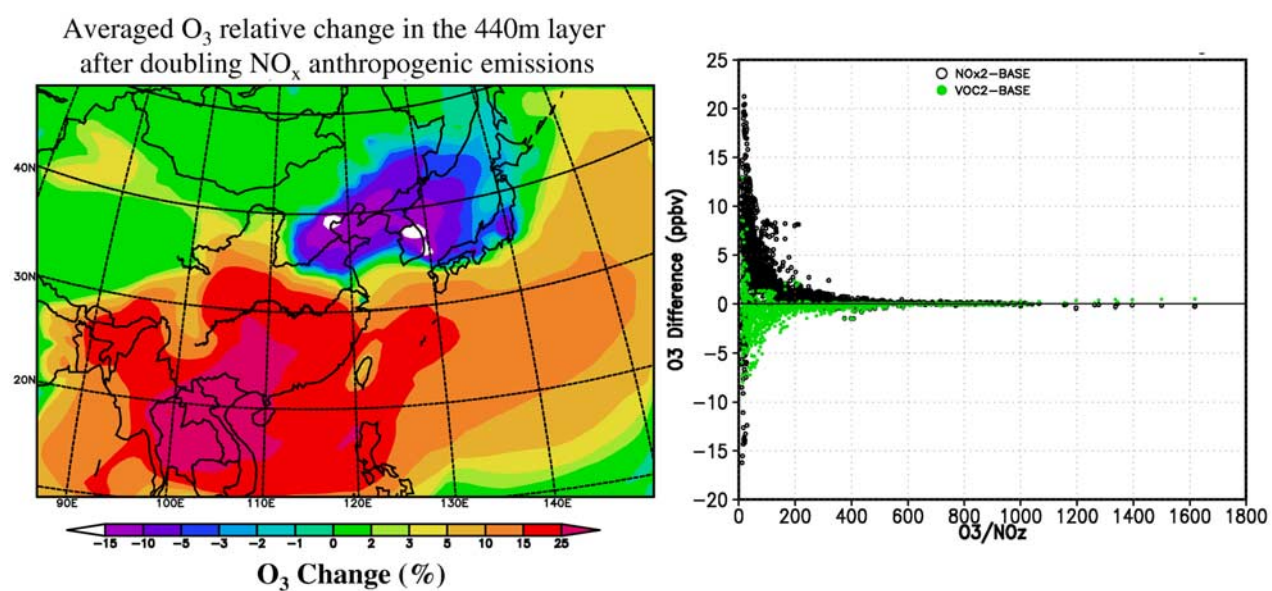
Figure 21. Average response in calculated ozone at ~500 m for the month of March due to a doubling in anthropogenic NO$_x$ emissions (left). The calculated response in ozone at the locations of the DC8 and P-3B aircraft observations for simulations where anthropogenic NO$_x$ and NMHC are increased by 2 times (separately) are also shown (right).